Monthly Notices
of the
ROYAL ASTRONOMICAL SOCIETY

MNRAS **475,** 1791–1808 (2018) doi:10.1093/mnras/stx3233
Advance Access publication 2017 December 14

The EDGE–CALIFA survey: the influence of galactic rotation on the molecular depletion time across the Hubble sequence

D. Colombo,[1⋆] V. Kalinova,[1⋆] D. Utomo,[2,3] E. Rosolowsky,[4] A. D. Bolatto,[5] R. C. Levy,[5] T. Wong,[6] S. F. Sanchez,[7] A. K. Leroy,[3] E. Ostriker,[8] L. Blitz,[2] S. Vogel,[5] D. Mast,[9] R. García-Benito,[10] B. Husemann,[11] H. Dannerbauer,[12,13] L. Ellmeier[14] and Y. Cao[6]

[1]*Max Planck Institute for Radioastronomy, Auf dem Hügel 69, D-53121 Bonn, Germany*
[2]*Department of Astronomy, University of California, Berkeley, CA 94720, USA*
[3]*Department of Astronomy, The Ohio State University, 140 West 18th Avenue, Columbus, OH 43210, USA*
[4]*Department of Physics, University of Alberta, 4-181 CCIS, Edmonton, AB T6G 2E1, Canada*
[5]*Department of Astronomy, University of Maryland, College Park, MD 20742, USA*
[6]*Department of Astronomy, University of Illinois, Urbana, IL 61801, USA*
[7]*Instituto de Astronomiá, Universidad Nacional Autonóma de Mexico, A.P. 70-264, 04510 México, D.F., Mexico*
[8]*Department of Astrophysical Sciences, Princeton University, Princeton, NJ 08544, USA*
[9]*Observatorio Astronómico de Córdoba, Laprida 854, Observatorio, X5000BGR Córdoba, Argentina*
[10]*Instituto de Astrofísica de Andalucía (CSIC), Glorieta de la Astronomía s/n, Aptdo. 3004, E-18080 Granada, Spain*
[11]*Max-Planck-Institut für Astronomie, Königstuhl 17, D-69117 Heidelberg, Germany*
[12]*Instituto de Astrofísica de Canarias, E-38205 La Laguna, Tenerife, Spain*
[13]*Dpto. Astrofísica, Universidad de La Laguna, E-38206 La Laguna, Tenerife, Spain*
[14]*Department of Astrophysics, University of Vienna, Türkenschanzstrasse 17, A-1180 Vienna, Austria*

Accepted 2017 December 7. Received 2017 December 6; in original form 2017 September 7

ABSTRACT

We present a kpc-scale analysis of the relationship between the molecular depletion time ($\tau_{\rm dep}^{\rm mol}$) and the orbital time ($\tau_{\rm orb}$) across the field of 39 face-on local galaxies, selected from the EDGE–CALIFA sample. We find that, on average, 5 per cent of the available molecular gas is converted into stars per orbital time, or $\tau_{\rm dep}^{\rm mol} \sim 20\,\tau_{\rm orb}$. The resolved relation shows a scatter of ∼0.5 dex. The scatter is ascribable to galaxies of different morphologies that follow different $\tau_{\rm dep}^{\rm mol}$–$\tau_{\rm orb}$ relations which decrease in steepness from early- to late types. The morphologies appear to be linked with the star formation rate surface density, the molecular depletion time, and the orbital time, but they do not correlate with the molecular gas content of the galaxies in our sample. We speculate that in our molecular gas rich, early-type galaxies, the morphological quenching (in particular the disc stabilization via shear), rather than the absence of molecular gas, is the main factor responsible for their current inefficient star formation.

Key words: ISM: molecules – galaxies: evolution – galaxies: kinematics and dynamics – galaxies: star formation – galaxies: structure.

1 INTRODUCTION

Star formation is the result of an intricate interplay of dynamical, thermal, radiative, and chemical phenomena that operates on a wide range of scales (McKee & Ostriker 2007; Padoan et al. 2014). Nevertheless, on a kpc scale, a simple 'recipe' for star formation emerges. This recipe was first formalized by Schmidt (1959), who suggested that the star formation rate (SFR) is proportional to the square of gas volume density (SFR $\propto \rho^2$). Afterwards, several works have aimed to empirically verify Schmidt's conjecture. The seminal studies were performed by Kennicutt (1989) and Kennicutt (1998), who measured the relation between the surface densities of SFR ($\Sigma_{\rm SFR}$) and total gas ($\Sigma_{\rm gas}$):

$$\Sigma_{\rm SFR} \propto \Sigma_{\rm gas}^{N}, \quad (1)$$

which goes by the name of the 'Kennicutt–Schmidt's relation' (hereafter the KS relation, also called 'star formation law') with $N = 1.40 \pm 0.15$. This relation can also be parametrized through

⋆ E-mail: dcolombo@mpifr-bonn.mpg.de (DC); kalinova@mpifr-bonn.mpg.de (VK)

© 2017 The Author(s)
Published by Oxford University Press on behalf of the Royal Astronomical Society

Downloaded from https://academic.oup.com/mnras/article-abstract/475/2/1791/4743749
by University of Durham - Stockton Campus user
on 13 March 2018

a single quantity called 'depletion time' which expresses the time-scale to convert the gas into stars at the current SFR:

$$\tau_{\rm dep} \equiv \frac{\Sigma_{\rm gas}}{\Sigma_{\rm SFR}}. \quad (2)$$

The inverse of $\tau_{\rm dep}$ is usually called the 'star formation efficiency' (SFE).

Resolved studies of nearby galaxies have shown that, on kpc-scales, the surface densities dominated by the molecular gas ($\Sigma_{\rm mol}$) linearly correlate with $\Sigma_{\rm SFR}$ (e.g. Bigiel et al. 2008; Leroy et al. 2008; Schruba et al. 2011; Leroy et al. 2013), while the atomic gas seems irrelevant (Wong & Blitz 2002; Heyer et al. 2004; Kennicutt et al. 2007; Schruba et al. 2011). The linearity means that the *molecular depletion time* is approximately constant: $\tau_{\rm dep}^{\rm mol} \approx 2$ Gyr (e.g. Leroy et al. 2008; Rahman et al. 2012; Leroy et al. 2013). However, most of these works are carried out in local discs, but studies of the integrated star-forming properties in high-redshift starburst (Daddi et al. 2010; Genzel et al. 2010; Tacconi et al. 2010) and quiescent early-type galaxies (Davis et al. 2014) show that not all systems follow the same KS relation as the nearby discs.

A relation explicitly incorporating the local orbital time (hereafter $\tau_{\rm orb}$) is able to describe the star formation in both high-redshift starbursts and nearby discs equally well (Daddi et al. 2010; Genzel et al. 2010) as proposed by Silk (1997) and Elmegreen (1997). This alternative 'star formation law' is sometimes called the 'Silk–Elmegreen' relation (hereafter SE relation). In particular, Silk (1997) defined the relation between $\Sigma_{\rm SFR}$ and $\Sigma_{\rm gas}$ as follows:

$$\Sigma_{\rm SFR} = \epsilon_{\rm orb} \frac{\Sigma_{\rm gas}}{\tau_{\rm orb}}, \quad (3)$$

where a fraction of gas, $\epsilon_{\rm orb}$ (hereafter: 'orbital efficiency'), is converted into stars during each orbital time.

Therefore, given the SE relation, a direct proportionality between the $\tau_{\rm dep}$ and $\tau_{\rm orb}$ is expected in the form:

$$\tau_{\rm orb} = \epsilon_{\rm orb} \tau_{\rm dep}. \quad (4)$$

Silk (1997) described equation (4) as a local relation with $\tau_{\rm dep} = \rho_{\rm gas}/\rho_{\rm SFR}$, where $\rho_{\rm gas}$ is the volumetric density of total neutral gas and $\rho_{\rm SFR}$ is the SFR volume density. Volume densities are difficult to measure in extragalactic context, but surface densities are more easily accessed. Thus, the original Silk (1997) relation is generally recast in term of equation (3). This relation can also be applied in global terms, assuming that neutral gas and young stars have similar scale height and radial distributions.

The intuition behind this relation originally relies on two different classes of models. Following the idea of Wyse (1986) and Wyse & Silk (1989), the multiple passages of clouds through regions of high gravitational potential (such as a spiral arm density-wave) favour the growth of clouds through collision and their subsequent collapse. Clouds on faster orbits (shorter orbital times) would encounter these gravitational depressions more frequently. As a consequence, the star formation rate and its efficiency within those objects will be enhanced with respect to clouds on slower orbits. In this case the star formation law would assume the form

$$\Sigma_{\rm SFR} \propto \Sigma_{\rm gas}^{N} (\Omega - \Omega_{\rm p}), \quad (5)$$

where $\Omega = V_{\rm c}/R_{\rm gal}$ is the disc angular speed and $\Omega_{\rm p}$ is the pattern speed of the spiral arms. In the limit where $\Omega_{\rm p}$ is small with respect to Ω (typically within the corotation) and $N = 1$, the star formation law assumes the form of the Silk–Elmegreen relation (equation 3), since $\tau_{\rm orb} = 2\pi/\Omega$.

Tan (2000) generalized this model to every episode of cloud compression, referring to negative shear as the main mechanism that supports the cloud coalescence in spiral arms (see also Tasker & Tan 2009; Tan 2010; Suwannajak, Tan & Leroy 2014). That model expressed the shear through the rotation curve shape factor $\beta = {\rm dln}\, V_{\rm c}/{\rm dln}\, R_{\rm gal}$ as

$$\Sigma_{\rm SFR} \propto \Sigma_{\rm gas} \Omega (1 - 0.7\beta). \quad (6)$$

For a flat circular velocity curve (CVC; $\beta = 0$), equation (6) is equivalent to the SE relation.

Alternatively, Wang & Silk (1994) predicted that the star formation rate scales with the total amount of gas divided by the time-scale for the perturbation growth in the disc, i.e.

$$\Sigma_{\rm SFR} \propto \Sigma_{\rm gas}/\tau_{\rm grow}. \quad (7)$$

The time-scale for the perturbation growth in a rotating disc can be expressed as (Tan 2000)

$$\tau_{\rm grow} \propto \sigma_{\rm gas}/\Sigma_{\rm gas} \propto Q/\kappa, \quad (8)$$

where $\sigma_{\rm gas}$ and $\Sigma_{\rm gas}$ represent the total gas velocity dispersion and the mass surface density, respectively. The Toomre (1964) Q-parameter indicates the ability of the gas to balance self-gravity with its own kinematics (parametrized via $\sigma_{\rm gas}$), together with centrifugal forces due to the disc rotation expressed through the epicyclic frequency κ. For a marginally stable disc, $Q \sim 1$ (or more generally Q is constant in a self-regulating star formation scenario) so that $\kappa \propto \Omega$, $\tau_{\rm grow} \sim \Omega^{-1} \propto \tau_{\rm orb}$. Thus, equation (7) has a similar form as equation (3). Global studies (Kennicutt 1998; Daddi et al. 2010; Genzel et al. 2010) implicitly assume that the orbital time, measured at the outer radius of the star-forming region, is equivalent to the average perturbation growth time-scale in the mid-plane of the disc.

Despite several successful observational applications (e.g. Kennicutt 1998; Boissier et al. 2003; Daddi et al. 2010; Genzel et al. 2010) and theoretical derivations (e.g. Tan 2000; Krumholz & McKee 2005; Narayanan et al. 2012), the direct proportionality between depletion time and orbital time implied by the SE relation has been often questioned. The resolved SE relation in M51 shows a significant scatter of 0.4 dex (Kennicutt et al. 2007) and systems of different physical scales are not well described by a single SE relation (e.g. Krumholz, Dekel & McKee 2012). Also, some theoretical works struggle to find such correlation (e.g. Dopita & Ryder 1994; Kim, Kim & Ostriker 2011).

The total gas depletion time of nearby galaxies appears proportional to the orbital time to some degree (Wong & Blitz 2002), but molecular depletion time ($\tau_{\rm dep}^{\rm mol}$) and $\tau_{\rm orb}$ are at most weakly correlated (Leroy et al. 2008; Wong 2009; Saintonge et al. 2011; Leroy et al. 2013). The correlation between $\tau_{\rm dep}^{\rm mol}$ and $\tau_{\rm orb}$ seems more significant in the inner region of the galaxies, where the orbital time becomes similar to the dynamical time of the GMCs (Leroy et al. 2013, see also Meidt et al. 2015).

Even with these difficulties and ambiguities, the orbital time remains a way to parametrize how large-scale dynamics influence the molecular gas properties at various levels. As seen above, there remains ample theoretical motivation to explore these influences and some suggestive observational evidences. In M51, flux and integrated intensity probability distribution functions show a strong deviation from a lognormal shape in the spiral arm region (Hughes et al. 2013). At the same time, streaming motions lengthen the molecular depletion time in the spiral arms of the galaxy (Meidt et al. 2013). The galactic disc differential rotation can set a limit to the development of expanding shells (Elmegreen, Palouš & Ehlerová

Downloaded from https://academic.oup.com/mnras/article-abstract/475/2/1791/4743749
by University of Durham - Stockton Campus user
on 13 March 2018

2002) and in the maximum mass that stellar clusters, GMCs, and high-redshift clumps can reach (Kruijssen 2014; Reina-Campos & Kruijssen 2017). These phenomena (together with stellar feedback) might be responsible for the different slope of the GMC mass spectra in M51 environments (Colombo et al. 2014), to create a large population of unbound clouds in the Milky Way and external galaxies (Dobbs & Pringle 2013; see also Dobbs, Burkert & Pringle 2011 and references therein), and to disperse the molecular gas to large scale height (Caldú-Primo et al. 2013; Pety et al. 2013).

Here, we expand the empirical study of the role of large-scale dynamics on molecular depletion time through a joint analysis of the Extragalactic Database for Galaxy Evolution (EDGE; Bolatto et al. 2017) and the Calar Alto Legacy Integral Field Area (CALIFA; Sánchez et al. 2012) surveys. This new analysis extends previous, resolved (kpc-scale) work on the local galaxy population to larger distances and a wider variety of galaxies. Furthermore, with the high-quality optical data, we are able to investigate what effects drive these relationships in the context of galaxy morphologies, stellar masses, and local properties. We focus on the parameter space defined by $\tau_{\rm dep}^{\rm mol}$ and $\tau_{\rm orb}$ using a sample of 39 approximately face-on spiral galaxies (inclination $<65^{\circ}$). Given the significantly wider exploration of parameter space we can complete a rich investigation of the different factors that could influence dynamically governed star formation.

The paper is organized as follows. In Section 2 we summarize the two surveys CALIFA (Section 2.1) and EDGE (Section 2.2) and the choice of sample (Section 2.3). Section 2.4 outlines the method we follow to obtain resolved maps of molecular depletion time from SFR and molecular gas surface densities, while in Section 2.5 we explore the theoretical basis to calculate circular speed models and orbital time per galactocentric radius from stellar kinematics. Section 3 reports the resolved relation analysed in the paper between $\tau_{\rm dep}^{\rm mol}$ and $\tau_{\rm orb}$ together with its corresponding integrated version. In Section 4 the pixel-by-pixel relations are encoded via the Hubble type and the stellar mass of the galaxies to study the global parameter dependence of the main quantities. Using the same properties, we show azimuthally averaged time-scale profiles of the different morphologies in Section 5. Finally, we discuss and summarize our findings (in Sections 6 and 7, respectively). We supplement the main work with appendices that test the influence of non-detections (Appendix A), local galaxy environment (Appendix B), and the influence of atomic gas (Appendix C) in the analysis of the depletion time, as well as a few additional caveats and limitations (Appendix D).

2 DATA AND SAMPLE

We make use of two data sets: the CALIFA survey (Sánchez et al. 2012), and the EDGE survey (Bolatto et al. 2017). Utomo et al. (2017) reports the method we used to derive SFR, molecular gas surface density, and molecular depletion time maps. The CVC models from stellar kinematics are calculated by Kalinova et al. (2017b), and the CO rotation curves are obtained by Levy et al. (in preparation). Detailed descriptions of those data products are presented in those papers. Here, we just provide a brief summary.

2.1 The CALIFA survey

CALIFA is a survey that observed more than 700 Sloan Digital Sky Survey (SDSS; York et al. 2002) galaxies in the local Universe through an integral field unit (IFU). The targets of CALIFA are chosen to be statistically representative of the galaxy population in the redshift range $0.005 < z < 0.03$. They cover a stellar mass range of $\log_{10}(M_*/[{\rm M}_\odot]) = 9.4$–$11.4$ (Walcher et al. 2014[1]); both early- and late-type morphologies, including mergers, and irregular galaxies (Sánchez et al. 2016). The data have been collected using the postdam multi-aperture spectrophotometer (PMAS) and the PMAS fibre PAcK (PPAK) IFU at the 3.5m telescope of the Calar Alto Observatory in Spain (García-Benito et al. 2015). The CALIFA sample is diameter-selected ($45\,{\rm arcsec} < D_{25} < 80\,{\rm arcsec}$), with a spatial resolution of 2.5 arcsec (corresponding to $\sim$1 kpc at the average redshift of the survey), and spans spectral ranges 3745–7300 Å ($R \sim 850$) and 3400–4750 Å ($R \sim 1650$). In terms of sample, CALIFA is more extended than previous, pioneering surveys (e.g. SAURON, Bacon et al. 2001; Atlas3D, Cappellari et al. 2011), which imaged mainly the centre of early-type, high-mass galaxies. At the same time, the PPAK instrument ensured large spatial coverage and number of fibres: CALIFA galaxies have better linear resolution than next-generation surveys (e.g. SAMI, Croom et al. 2012; Bryant et al. 2015; and MaNGA, Bundy et al. 2015; Sánchez et al. 2016). CALIFA represents, to date, the best trade-off between sample statistics and survey design among IFU surveys.

In our analysis of CALIFA data, we use emission line maps (at Hα, Hβ, [N II], [O III] wavelengths), stellar population synthesis products, and stellar kinematic results (provided by the PIPE3D pipeline described in Sánchez et al. 2016). These maps are regridded and smoothed to match the pixel scale and resolution of EDGE data. Low signal-to-noise ratio pixels (SNR <2) are blanked as well as foreground stars (see Utomo et al. 2017 for details).

2.2 The EDGE survey

EDGE is the ^{12}CO $J = 1$–0 and ^{13}CO $J = 1$–0 follow-up survey of 177 infrared-bright CALIFA galaxies. Among those, 126 targets have been observed with both D+E configurations of CARMA, yielding a typical synthesized beam of $\sim$4.5 arcsec. Given the average distance of EDGE targets, this resolution corresponds to approximately 1.5 kpc. The D+E cubes used in this analysis have a channel width of 10 km s^{-1}. The RMS noise in EDGE cubes ranges between 40 and 65 mK with an average of $\sim$50 mK, giving a $3\sigma_{\rm RMS}$ sensitivity of $\Sigma_{\rm mol} \sim 11\,{\rm M}_\odot\,{\rm pc}^{-2}$ (before inclination corrections). EDGE is by far the most extended interferometric ^{12}CO(1–0) survey in the local Universe. It spans broader ranges of colour, luminosity, stellar masses, and morphological types than the previous kpc-scale surveys which focused on nearby, blue, star-forming galaxies (e.g. BIMA SONG, Regan et al. 2001; Helfer et al. 2003; HERACLES, Leroy et al. 2009; CARMA STING, Rahman et al. 2011; Rahman et al. 2012) or the centres of early-type galaxies (Alatalo et al. 2013). Full information about the EDGE survey design and data reduction appeared in Bolatto et al. (2017).

In our studies, we use moment maps from D+E data cubes, masked in order to capture CO emission. The signal-to-noise ratio in pixels within the mask is mostly SNR >2. Those masks have been constructed using the Interactive Data Language (IDL) method developed by Wong et al. (2013).[2] To minimize oversampling, the

[1] The mass range has been originally calculated by Walcher et al. (2014) using a Chabrier (2003) initial mass function (IMF). Throughout the paper we adopt a Kroupa (2001) IMF (see also Utomo et al. 2017). By assuming the conversion factor suggested by Madau & Dickinson (2014), $\rm IMF_{Kroupa} = 1.07\,IMF_{Chabrier}$; therefore, the indicated mass range is consistent with our assumed IMF.

[2] https://github.com/tonywong94/idl_mommaps

Downloaded from https://academic.oup.com/mnras/article-abstract/475/2/1791/4743749
by University of Durham - Stockton Campus user
on 13 March 2018

Table 1. The sample of nearby EDGE–CALIFA galaxies considered in this work: (1) CALIFA name of the galaxies; (2) Hubble type defined by eye from members of the CALIFA team as described in Walcher et al. 2014. In the paper we group different elliptical types in the same category 'E', S0 and S0a galaxies are considered as 'S0' type, while Sdm galaxies are grouped together to 'Sd' types; (3) median and median absolute deviation of the detected lines of sight from the SFR surface density map of a given galaxy; (4) median and median absolute deviation of the detected lines of sight from the molecular gas mass surface density map of a given galaxy; (5) median and median absolute deviation of the detected lines of sight from the molecular depletion time map of a given galaxy; (6) median and median absolute deviation of the orbital time where both Σ_{SFR} and Σ_{mol} are detected; (7) median and median absolute deviation of the local shear rate (Oort's A) where both Σ_{SFR} and Σ_{mol} are detected; (8) effective radius measured by Walcher et al. 2014; (9) inclination from CO kinematics (Levy et al., in preparation); (10) distance from HyperLEDA; (11) number of detected τ_{dep}^{mol} lines of sight (both Σ_{SFR} and Σ_{mol} detected with SNR >2); (12) number of non-detected τ_{dep}^{mol} lines of sight (either Σ_{SFR} or Σ_{mol} have SNR <2).

Galaxy	Hubble type	Σ_{SFR} (10^{-4} $M_\odot$ kpc^{-2} yr^{-1})	Σ_{mol} ($M_\odot$ pc^{-2})	τ_{dep}^{mol} (10^9 yr)	τ_{orb} (10^8 yr)	A (10^{-8} yr^{-1})	R_{eff} (arcsec)	i (°)	D (Mpc)	N_{los}^{det}	$N_{los}^{non-det}$
(1)	(2)	(3)	(4)	(5)	(6)	(7)	(8)	(9)	(10)	(11)	(12)
NGC6021	E5	0.65 ± 0.01	19.56 ± 0.69	302.53 ± 7.28	2.41 ± 0.07	1.23 ± 0.04	11.18	43	69	2	14
NGC5485	E5	1.4 ± 0.1	13.31 ± 1.56	109.11 ± 20.46	0.53 ± 0.08	1.89 ± 0.21	15.79	47	27	7	32
NGC5784	S0	136.47 ± 64.47	24.83 ± 8.31	2.52 ± 1.13	0.69 ± 0.22	4.28 ± 1.06	12.04	45	79	73	148
...	...	...	...	...	...	...	...	...	...	...	
...	...	...	...	...	...	...	...	...	...	...	
...	...	...	...	...	...	...	...	...	...	...	
NGC3381	Sd	165.1 ± 81.93	21.98 ± 4.68	1.47 ± 0.76	1.53 ± 0.69	0.35 ± 0.08	21.42	31	23	59	209

original EDGE images have been regridded so that each independent resolution element corresponds to 4 pixels (Utomo et al. 2017). This sampling is used throughout this paper.

2.3 Sample selection

The sample considered in this paper consists of 83 objects, which is the overlap between 126 galaxies from the full EDGE D+E sample and the 238 CALIFA galaxies that have the CVC modelled by Kalinova et al. (2017b). The sample list is provided in Table 1 along with some other useful information regarding our galaxies. In most of the analysis, we only use galaxies with inclination below 65°. We explore the effect of inclinations in highly inclined galaxies in Appendix D. There are 71 EDGE galaxies with inclination below this 65° limit, which, when restricted to the samples with dynamical models and that encompass at least one line of sight with SNR >2 (for both Σ_{SFR} and Σ_{mol}) results in 39 objects. Fig. 1 shows the comparison between the parent EDGE sample (after inclination cut) and the sample used in this paper. Although there is a significant reduction in the number of galaxies, our sample is still a representation of the EDGE sample (after inclination cut) in terms of the Hubble type, stellar masses, star formation rates, and molecular gas masses. However, very late-type galaxies (Sd) are underrepresented in our sample. Galaxies with $\log(SFR/M_\odot\ yr^{-1}) > 1$ and $\log(M_{mol}/M_\odot) > 10$ are also underrepresented with respect to the EDGE sample (after inclination cut).

2.4 Molecular depletion time maps

The maps of molecular depletion time have been generated by Utomo et al. (2017) and they are fully described there. Here, we give a short summary of their derivation method. The molecular depletion time is calculated by

$$\tau_{dep}^{mol} = \frac{\Sigma_{mol}}{\Sigma_{SFR}}. \quad (9)$$

The deprojected maps of molecular gas surface density (Σ_{mol}) are generated by following Leroy et al. (2008):

$$\frac{\Sigma_{mol}}{M_\odot\ pc^{-2}} = \alpha_{CO}\ \cos i\ \frac{I_{CO}}{K\ km\ s^{-1}}, \quad (10)$$

where we assume the Galactic CO-to-H_2 conversion factor of $\alpha_{CO} = 4.4$ to convert between ^{12}CO (J = 1–0) integrated intensity (I_{CO}) to Σ_{mol}; $\cos i$ accounts for the deprojected area due to the inclination (i) of galaxies.

The maps of star formation rate surface density (Σ_{SFR}) are obtained from

$$\Sigma_{SFR}(M_\odot\ pc^{-2}\ yr^{-1}) = C \times \frac{4\pi d^2 F(H_\alpha) \cos i}{S_{pix}} \times 10^{0.4\ A_{H_\alpha}}. \quad (11)$$

The Hα flux maps (F(Hα)) are converted to Hα luminosity by considering the distance d of the galaxies in pc, which are drawn from the HyperLEDA catalogue (Makarov et al. 2014). The nebular extinction of Hα ($A_{H\alpha}$) is calculated applying the Balmer decrement method (e.g. Catalán-Torrecilla et al. 2015, equation 1), which compares the observed and theoretically expected ratios between Hα and Hβ fluxes. To convert between extinction-corrected Hα luminosities and SFR, we use the calibration factor $C = 5.3 \times 10^{-43}$ ($M_\odot$ yr^{-1} erg^{-1} s) from Calzetti et al. (2007). Finally, SFR surface density maps are generated by dividing SFR by the physical pixel area of the regridded and deprojected Hα flux maps, S_{pix}, expressed in kpc. Additionally, we blank the AGN-like emission pixels that lie above the Kewley & Dopita (2002) relation in the Baldwin, Phillips & Terlevich 1981 (BPT) diagram (constructed by the [N II]/Hα and [O III]/Hβ line ratio maps) as well as pixels with Hα equivalent width <6Å, because this Hα emission is caused by stars older than 500 Myr, which are not associated with star formation (Sánchez et al. 2014).

Pixels within Σ_{SFR} and Σ_{mol} maps with SNR >2 are considered as detections in our analysis. Following Utomo et al. (2017), we will also study what we consider as upper and lower limits of the depletion time. Upper τ_{dep}^{mol} limits are measured by including non-detections in Σ_{mol} as $2\sigma_{rms}$ values. The uncertainty level within the masked cube ($1\sigma_{rms}$) is calculated as the standard deviation of the noise along the velocity axis. The lower limits are given by the non-detections of the SFR surface density. We considered non-detections in Σ_{SFR} as values below $2\sigma_{rms}$, where the noise level ($1\sigma_{rms}$) is determined by the median absolute deviation of the AGN-masked CALIFA Hα maps.

Downloaded from https://academic.oup.com/mnras/article-abstract/475/2/1791/4743749
by University of Durham - Stockton Campus user
on 13 March 2018

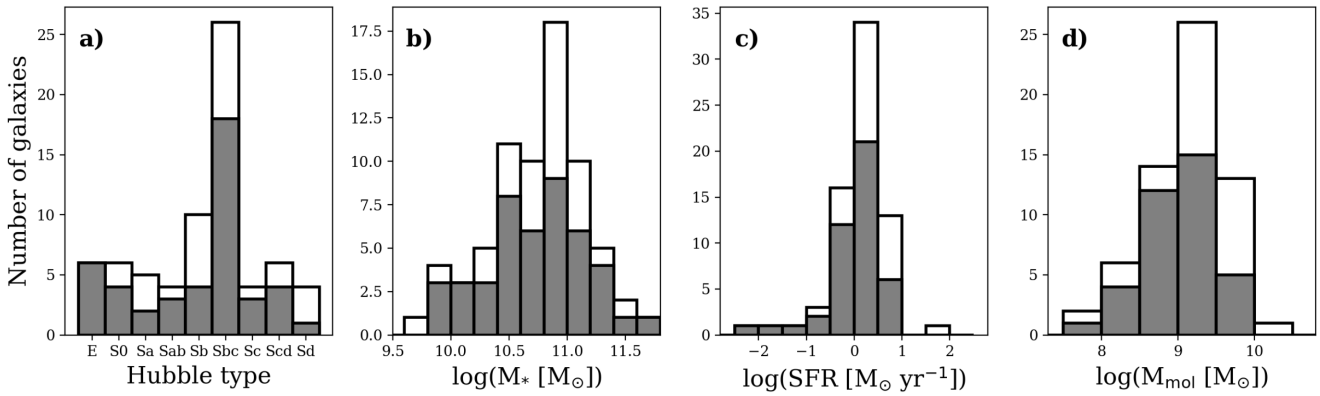

Figure 1. The histograms of Hubble types (panel a; Walcher et al. 2014), integrated stellar masses (panel b; Sánchez et al. 2016), SFR (panel c; Bolatto et al. 2017), and molecular gas masses (panel d; Bolatto et al. 2017) of the full EDGE D+E sample (white) and the sample in this paper (grey). Both samples are restricted to galaxies with inclination below 65°. This figure shows that the sample that is selected for this study is still representative of the full EDGE sample of Bolatto et al. (2017).

2.5 Dynamical models, circular velocity curves, and orbital times

We calculate the orbital times from the CVCs inferred from stellar kinematics and SDSS *r*-band surface brightness (Kalinova et al. 2017b), rather than from the CO rotation curve. This choice maximizes the dynamic ranges of stellar masses and Hubble types in our sample, because the rotation curves inferred from CO are mainly available for intermediate morphological types (Levy et al., in preparation). Since stars are present in all galaxy types, we can obtain orbital times for EDGE targets that are barely resolved in CO emission without being constrained by the accuracy of their CO rotation curves. A similar approach has been used by Davis et al. (2014) to calculate rotation curves for a sample of fast rotating early-type galaxies.

The CVCs were derived using the axis-symmetric case of Jeans anisotropic multi-Gaussian expansion dynamical model (JAM;[3] Cappellari 2008). In the JAM approach, two basic assumptions are made for the stellar population: a constant velocity anisotropy ($\beta_z = 1 - \sigma_z^2/\sigma_R^2$) and a constant dynamical mass-to-light ratio ($\Upsilon_{\rm dyn}$). The parameters β_z and $\Upsilon_{\rm dyn}$ have been defined after fitting the observed second-order velocity moment $V_{\rm rms} = \sqrt{V^2 + \sigma^2}$ calculated from the stellar kinematics of the galaxies (Falcón-Barroso et al. 2017). The best-fitting model of the observed $V_{\rm rms}$, the corresponding fitting parameters (β_z and $\Upsilon_{\rm dyn}$), and their uncertainties are obtained by applying the Markov Chain Monte Carlo method as described in Kalinova et al. (2017a).

The CVC is derived by applying Poisson's equation to the best fit of gravitational potential $\Phi(R, z)$. $\Phi(R, z)$ is generated via the multi-Gaussian expansion method (MGE; Monnet, Bacon & Emsellem 1992; Emsellem, Monnet & Bacon 1994), where the observed surface brightness of the galaxies is parametrized as a sum of N Gaussian components, which represent the photometry of the galaxies in detail, as follows:

$$I(x', y') = \sum_{j=0}^{N} I_{0,j} \exp\left\{-\frac{1}{2\xi_j'^2}\left[x'^2 + \frac{y'^2}{q_j'^2}\right]\right\}, \quad (12)$$

where $I_{0,j}$ is the central surface brightness, ξ_j' is the dispersion along the major x'-axis and q_j' describes the flattening of the ellipses. The intrinsic dispersion ξ_j and flattening q_j are related to their observed (plane-of-sky) equivalents to

$$\xi_j = \xi_j' \quad \text{and} \quad q_j'^2 = \cos^2 i + q_j^2 \sin^2 i. \quad (13)$$

Kalinova et al. (2017b) obtained the MGE models using the software implementation of Cappellari (2002). The code was applied to the *r*-band photometric images from the SDSS using Data Release 12 (Alam et al. 2015).

Finally, the circular velocity from the JAM model is derived from (e.g. section 3.2. of Kalinova et al. 2017a):

$$V_{\rm c}^2(R_{\rm gal}) \equiv V_{\rm c,JAM}^2(R_{\rm gal}) = \sum_{j=0}^{N} \frac{2\,G L_j \Upsilon_j}{\sqrt{2\pi}\xi_j} \frac{R_{\rm gal}^2}{\xi_j^2} \times \int_0^1 \exp\left\{-\frac{u^2 R_{\rm gal}^2}{2\xi_j^2}\right\} \frac{u^2\,{\rm d}u}{\sqrt{1-(1-q_j^2)u^2}}, \quad (14)$$

where $L_j \equiv 2\pi\xi_j^2 q_j' I_{0,j}$ and Υ_j are the total luminosity and the mass-to-light ratio of the jth Gaussian. Due to the assumption of a constant mass-to-light ratio, Υ_j is taken to be the same for all Gaussians in the dynamical model, i.e. $\Upsilon_j = \Upsilon_{\rm dyn}, \forall j$ (see Section 3.2 of Kalinova et al. 2017a).

Given the CVC, we can compute the orbital time at each galactocentric radius $R_{\rm gal}$ as

$$\tau_{\rm orb}({\rm yr}) = \frac{2\pi R_{\rm gal}}{V_{\rm c}(R_{\rm gal})}. \quad (15)$$

The orbital time is a proxy for the depth of the global potential well of the galaxies within $R_{\rm gal}$. We ensure that all galaxies in our sample are fast rotators by performing the test described in Emsellem et al. (2011) equation (3), where galaxy ellipticity and angular momentum are calculated by Kalinova et al. (2017b) (see also Falcón-Barroso et al. 2017). Moreover, JAM circular speeds are largely in agreement with the CO rotation curves. Comparing JAM models to CO curves only reveals small differences (typically $\sim$10 km s^{-1}; Leung et al., submitted), despite the assumption of a constant $\Upsilon_{\rm dyn}$ that has been shown to be not completely appropriate for galactic discs (de Denus-Baillargeon et al. 2013). $\tau_{\rm orb}$ estimates reflect the orbital times within the molecular gas in the mid-plane. Nevertheless, we discuss in Appendix D possible biases introduced by the JAM modelling in the $\tau_{\rm dep}^{\rm mol}$–$\tau_{\rm orb}$ relation.

[3] http://www-astro.physics.ox.ac.uk/mxc/software/#jam

Downloaded from https://academic.oup.com/mnras/article-abstract/475/2/1791/4743749
by University of Durham - Stockton Campus user
on 13 March 2018

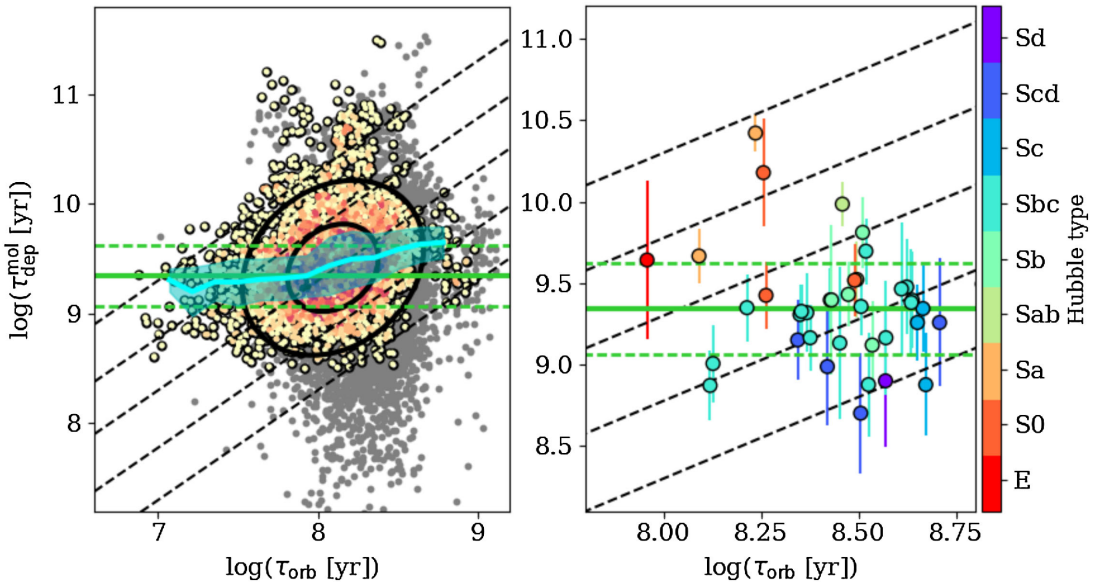

Figure 2. *Left*: The resolved relationship between $\tau_{\rm dep}^{\rm mol}$ and $\tau_{\rm orb}$ in our EDGE–CALIFA sample. This figure shows that the detected lines of sights cluster around the 5 per cent orbital efficiency with a large scatter of 0.5 dex. Coloured circles in the diagrams refer to the detections only, with darker colours represent higher number densities of pixels. The upper and lower limits of $\tau_{\rm dep}^{\rm mol}$ are indicated as grey points. Black ellipses mark the 1σ (inner) and 2σ (outer) confidence interval of the data, derived from the principal component analysis (see the text). The cyan line and its band indicate the median and interquartile range of $\tau_{\rm dep}^{\rm mol}$ within bins of 0.2 dex in $\tau_{\rm orb}$. *Right*: The integrated measurements of the molecular depletion times (calculated within $2\,R_{\rm eff}$) and the orbital times (measured at $2\,R_{\rm eff}$). The measurements of $\tau_{\rm dep}^{\rm mol}$ and $\tau_{\rm orb}$ in Sb–Sbc galaxies (which dominate our sample) are moderately correlated (Spearman rank $\sim$0.7) and show a median orbital efficiency of 10 per cent, while other Hubble type galaxies largely deviate from this value. Considering measurements within different effective radii does not change the general trend with the Hubble types that we show in this figure. In both panels, parallel dashed black lines represent loci where a certain fraction of molecular gas is consumed by star formation at each orbit (orbital efficiency, $\epsilon_{\rm orb}$): 0.5 per cent, 1.7 per cent, 5 per cent, 17 per cent, and 50 per cent (from top to bottom). As a comparison, the horizontal solid green line marks the average depletion time of 2.2 Gyr as measured in nearby spiral galaxies by Leroy et al. 2013, together with their scatter of $\pm$0.28 dex (dashed green lines).

3 A RELATION BETWEEN THE RESOLVED MOLECULAR DEPLETION AND ORBITAL TIMES FROM LOCAL GALAXIES?

Identifying the connections between the molecular depletion time and other time-scales in the galaxies can give insight into the physics that regulates the star formation. The orbital time is the longest of the relevant dynamical times in the galactic discs (see e.g. Semenov, Kravtsov & Gnedin 2017, and references therein), therefore it is the closest in magnitude to typical molecular depletion time values measured on kpc-scale. Here, we explore the connections between molecular depletion time and orbital time using resolved measurements from EDGE and CALIFA data. Fig. 2 (left) shows the result of the analysis as a bi-dimensional histogram. The data are largely scattered around the following values:

(i) $\tau_{\rm orb} = (3.2^{+2.0}_{-1.2}) \times 10^8$ yr,
(ii) $\tau_{\rm dep}^{\rm mol} = (2.8^{+2.3}_{-1.2}) \times 10^9$ yr,

where the characteristic values are the median of the respective distributions, and the scatter is given by the interquartile range, spanning the 25th to 75th percentiles of the distributions. Beside the difference in order of magnitude, the depletion and orbital times show similar dynamic ranges. Molecular depletion time values are largely in agreement with the results of Leroy et al. (2013) which measure a $\tau_{\rm dep}^{\rm mol} = (2.2^{+2.0}_{-1.0}) \times 10^9$ yr. Their sample, however, does not include early-type galaxies, which can shift the $\tau_{\rm dep}^{\rm mol}$ median to higher values. In the panel, the two concentric 1σ and 2σ confidence ellipses approximate the regions of the diagram that contain $\sim$68 per cent and $\sim$95 per cent of the data, respectively; oriented in the direction of maximal variance of the data points. Those ellipses are obtained by performing a principal component analysis (PCA) of the data. The PCA technique (Pearson 1901) constructs the covariance matrix of the data and performs a spectral embedding of the matrix in order to describe the data through their larger variance direction. The confidence ellipsoids are oriented by the main eigenvector of the matrix (i.e. the eigenvector with the largest eigenvalue) which indicates the direction of maximum extension of the data in the plane. The orientation of the main eigenvector defines, in essence, the *slope* of the relation under analysis. The major and minor axes of the ellipsoid are calculated as $\sigma_{\rm maj,min} = 2\sqrt{\lambda_{\rm maj,min}}$, where $\lambda_{\rm maj,\,min}$ indicate the largest and the smallest eigenvectors of the matrix, respectively. In this case, $\sigma_{\rm min}$ represents the *scatter* of the relation. The angle between the ellipses and the x-axis is $\sim$70° (equivalent to a slope $\sim$3.4), indicating that the relation between the two $\tau_{\rm dep}^{\rm mol}$ and $\tau_{\rm orb}$ is much steeper than linear. Also, the two quantities are not strongly correlated given that the ratio between the 1σ ellipse major and minor axes is $\sim$1.5. Despite the scatter, an orbital efficiency of $\epsilon_{\rm orb} = 5$ per cent describes quite well the trend in the data and follows the median of the data within the 1σ ellipse. The 1σ ellipse is bounded by the $\epsilon_{\rm orb} = 1.7$ per cent and $\epsilon_{\rm orb} = 17$ per cent lines. Globally therefore the resolved measurements of depletion time appear to follow equation (4) (restricted to the molecular gas mass surface density) with $\epsilon_{\rm orb} = 5$ per cent and a scatter of about $\sim$0.5 dex; in other words 5 per cent of the available molecular gas is converted into stars at each orbit in our galaxies. The data are asymmetrically scattered around the outer confidence ellipse towards high values of depletion time, probably due to the shortage of late-type galaxies in our

Downloaded from https://academic.oup.com/mnras/article-abstract/475/2/1791/4743749
by University of Durham - Stockton Campus user
on 13 March 2018

sample. Our orbital efficiency value is comparable to other results from local galaxies in the literature which found $\epsilon_{\rm orb} \sim 6-7$ per cent (Kennicutt 1998; Wong & Blitz 2002; Leroy et al. 2008). Nevertheless, a clear correlation between molecular depletion time and orbital time is rarely observed (e.g. Wong 2009; Leroy et al. 2008) especially in the molecular-dominated regime (Leroy et al. 2008). In order to check the impact of $\Sigma_{\rm mol}$ and $\Sigma_{\rm SFR}$ non-detections, we include upper and lower limits of the molecular depletion time in the plots (grey points). By adding those values, the relation between $\tau_{\rm dep}^{\rm mol}$ and $\tau_{\rm orb}$ becomes highly questionable, since many low molecular depletion time points are added. Those values are mostly due to $\Sigma_{\rm mol}$ non-detections (see Appendix D).

Originally, the relation between depletion time and orbital time has been tested indirectly by Kennicutt (1998) using total gas mass surface densities and integrated measurements. In his study, the assumed orbital time was measured at the outer edge of the star-forming region and it was used as dynamical time in his version of the Schmidt's law. The author concluded that the Schmidt's relation, modified to account for the orbital time, provides a feasible star formation law. Kennicutt (1998) measured an orbital efficiency of 10 per cent in a sample of normal spiral plus starburst galaxies. Following this seminal work, we use the orbital time measured at $2\,R_{\rm eff}$, together with molecular depletion times integrated within the same radius (Fig. 2, right). Additionally, we colour-encode the data points by the Hubble type of their galaxies. The morphology of our galaxies has been defined by-eye by members of the CALIFA teams as described in Walcher et al. (2014). Sbc galaxies which, in number, dominate our sample (we have 18 Sbc on a total of 39 objects) appears to cluster around $\epsilon_{\rm orb} \sim 10$ per cent. Moreover the data points belonging to these galaxies appear moderate correlated showing a Spearman rank $\sim$0.7. Including the Sb galaxies (which follow the same orbital efficiency of 10 per cent) the Spearman rank decreases to 0.5. Nevertheless, other type galaxies largely deviate from this value. In particular the early types (e.g. E, S0, and Sa types) show very long depletion times, away from the main relation. Across the Hubble sequence global measurements of $\tau_{\rm dep}^{\rm mol}$ and $\tau_{\rm orb}$ appear actually anticorrelated. A similar anticorrelation has been noticed by Leroy et al. (2013) (see their fig. 7) for a different sample of nearby discs, which, as in our case, include only molecular gas.

For comparison with the analysis of Kennicutt (1998) and Leroy et al. (2008), we simulate the effects of including atomic gas in our analysis. The results of the test, reported in Appendix C, suggest that considering the atomic gas might not significantly alter the appearance of both pixel-by-pixel and integrated depletion time–orbital time relationships in our molecular-rich galaxies.

4 RESOLVED ORBITAL TIME RELATIONSHIPS ACROSS MORPHOLOGIES AND MASSES

In the previous section, we show that the resolved $\tau_{\rm dep}^{\rm mol}$ and $\tau_{\rm orb}$ measurements from our sample of EDGE–CALIFA galaxies cluster around an orbital efficiency of 5 per cent, albeit with a scatter of 0.5 dex. In addition, we showed that the integrated molecular depletion times in early-type galaxies deviate from the $\tau_{\rm dep}^{\rm mol}$–$\tau_{\rm orb}$ relation of the later type galaxies. In this regard, we want to test if the scatter in the resolved $\tau_{\rm dep}^{\rm mol}$–$\tau_{\rm orb}$ relationship is attributable to the Hubble type by colour-encoding the detected line of sight by their morphologies. The result of this analysis is shown in Fig. 3, where we also consider $\Sigma_{\rm SFR}$ and $\Sigma_{\rm mol}$ versus $\tau_{\rm orb}$. When the galaxies are segregated through the Hubble types, the medians of the depletion and orbital times reflect the behaviour of the integrated measurements, i.e. the kpc-size regions in the early-type galaxies have longer depletion times, but shorter orbital times with respect to the late types (Fig. 3a). In particular, the medians for Sb–Sbc galaxies lie exactly on the $\epsilon_{\rm orb} = 5$ per cent locus. Even though the averaged $\Sigma_{\rm SFR}$ and $\tau_{\rm orb}$ correlate with morphologies (Fig. 3b), it is not true for $\Sigma_{\rm mol}$, where the distribution of median values appear to be packed at the same location (Fig. 3c). Those trends are more prominent if non-detections are included (see Appendix A).

Additionally, different Hubble types appear to follow different $\tau_{\rm dep}^{\rm mol}$–$\tau_{\rm orb}$ relations relative to from the global trend (Fig. 3a). For earlier types (e.g. S0, Sa, Sab) the correlations are steep. This steepness decreases in the late types (e.g. Sc, Scd, and Sd). For Sb galaxies, the molecular depletion time appears to be uncorrelated with $\tau_{\rm orb}$. The latter result is consistent with comparable, kpc-scale, resolved studies (e.g. Leroy et al. 2008; Wong 2009; Leroy et al. 2013; which include late spirals only) that do not identify a significant trend between the two quantities. The difference in the steepness of the $\tau_{\rm dep}^{\rm mol}$–$\tau_{\rm orb}$ relation with the Hubble types seems to be driven by the behaviour of $\Sigma_{\rm SFR}$ with the orbital time. Indeed, the $\Sigma_{\rm SFR}$–$\tau_{\rm orb}$ relationship flattens from early- to late types, while $\Sigma_{\rm mol}$ and $\tau_{\rm orb}$ are anticorrelated, but, modulo outliers, no significant variations with the Hubble types are observed. Therefore, regarding our sample, the different behaviours of molecular depletion time with respect to orbital time and galaxy morphology are mostly driven by the correlations of SFR surface densities with these two parameters ($\tau_{\rm dep}^{\rm mol}$ and $\tau_{\rm orb}$).

Similarly, data points corresponding to different Hubble types are well localized in particular regions of the diagrams. Regions above the nearby galaxy depletion time ($\tau_{\rm dep}^{\rm mol} \sim 2$ Gyr) and above the sample running average are mostly populated by early-type galaxies (e.g. E, S0, and Sa). Elliptical galaxies, for which we possess only a few measurements, show very large values of depletion time ($\tau_{\rm dep}^{\rm mol} > 10^{11}$ yr). The early-type galaxies seem to have somewhat shorter orbital times than others. Sab, Sb, and Sbc span larger regions of the $\tau_{\rm dep}^{\rm mol}$–$\tau_{\rm orb}$ diagram, where the depletion time decreases from Sab to Sbc types, reaching value of an order of magnitude below the sample average and the nearby galaxy value. At the same time, late-type galaxies show longer orbital time compared to the early types ($\tau_{\rm orb} > 10^{8.5}$ yr) that slowly increases from Sab to Sbc. Nevertheless, those galaxy morphologies cover the largest area of the $\tau_{\rm dep}^{\rm mol}$–$\tau_{\rm orb}$ diagram. Most of the late-type galaxy molecular depletion times (e.g. Scd and Sd) are, instead, below the average. For these galaxies orbital times span a large range ($10^{6.5} < \tau_{\rm orb} < 10^{9.2}$ yr).

If we consider the average orbital efficiency of the full sample (i.e. $\epsilon_{\rm orb} = 5$ per cent), the scatter of the detected lines of sight across the Hubble sequence decreases: $\sim$2 dex for E galaxies, $\sim$0.7 dex for S0, Sa, and Sab galaxies; and $\sim$0.3–0.4 dex for galaxies between Sb to Sd types.

González Delgado et al. (2015) clearly showed that the stellar mass of galaxies decreases along the Hubble sequence (see their Fig. 2). To understand whether the correlations with morphology are merely a reflection of the stellar mass behaviour, in the second row of Fig. 3 we group the lines-of-sight within bins of 0.2 M_* dex. Stellar masses are obtained from the product of stellar population synthesis of Sánchez et al. (2016) (after converting from Salpeter to Kroupa IMF). Fig. 3 d shows that the molecular depletion time increases with increasing stellar mass. High stellar masses ($M_* > 10^{11}\,{\rm M}_\odot$) correspond to $\tau_{\rm dep}^{\rm mol} \gtrsim 10^9$ yr, while low-mass galaxy data span the full parameter space: galaxies with stellar masses $<10^9\,{\rm M}_\odot$ can also have $10^{8.5} < \tau_{\rm dep}^{\rm mol} < 10^{11}$ yr. This result resembles what was found by Bolatto et al. (2017; see their fig. 18), where galaxies with

Downloaded from https://academic.oup.com/mnras/article-abstract/475/2/1791/4743749
by University of Durham - Stockton Campus user
on 13 March 2018

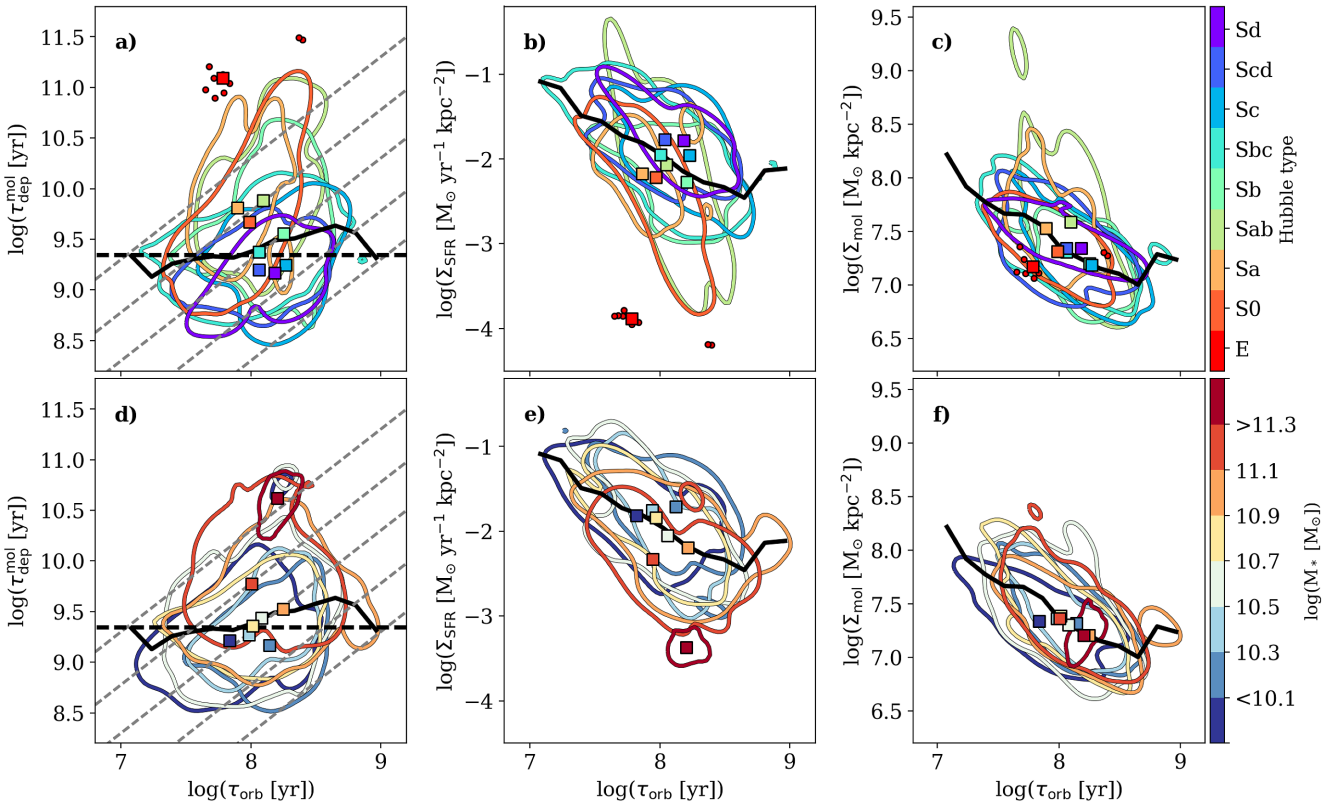

Figure 3. Pixel-by-pixel relations between τ_{dep}^{mol} (first column), Σ_{SFR} (second column), and Σ_{mol} (third column) with respect to τ_{orb}, where both Σ_{SFR} and Σ_{mol} are detected with line-of-sight SNR >2. The data are colour-encoded by Hubble type (first row) and integrated stellar mass (second row). The coloured contours indicate the kernel density estimation (KDE)-smoothed surface that contains 95 per cent of the points in a given category. Elliptical galaxies, for which we possess only few line of sights, are plotted with red circles, instead of a contour. Coloured squares indicate the positions of the quantity medians for each category. The black solid lines indicate the medians of the related quantities within 0.2 dex bins of orbital times. The black horizontal dashed lines in panels (a) and (d) mark the nearby star-forming galaxy depletion time of 2.2 Gyr (Leroy et al. 2013), while the grey diagonal lines are the constant orbital efficiencies (from left to right) of 0.5 per cent, 1.7 per cent, 5 per cent, 17 per cent, and 50 per cent. This figure shows that the τ_{dep}^{mol}–τ_{orb} and Σ_{SFR}–τ_{orb} relations (panels a and a) are segregated by the Hubble types, in the sense that the slopes of the relation are shallower from early to late-type galaxies. However, these trends cannot be simply attributed to the different stellar masses of galaxies (panels d and e) nor the molecular gas surface density (panels c and f).

stellar mass above (below) $M_* = 10^7\,M_\odot$ appear to dominate the depletion time values above (below) the full sample τ_{dep}^{mol} median (see also Fig. 3d).

Nevertheless, the trend of the distribution of medians in the various diagrams is less clear when segregated through stellar mass bins. The depletion and orbital times are weakly correlated across the stellar masses (Fig. 3d), as well as Σ_{SFR} and τ_{orb} which seems to be anticorrelated in the same representation (Fig. 3e). As for the galaxy morphologies, we do not distinguish any clear trends when Σ_{mol} is considered (Fig. 3f).

Data points within different M_* bins do not follow different τ_{dep}^{mol}–τ_{orb} relationships as for the Hubble type. The behaviour of the depletion time with the stellar mass seems to be driven mostly by the SFR per unit area that clearly decreases with increasing stellar mass. Again, data points corresponding to low-mass galaxies ($M_* < 10^9\,M_\odot$) span all Σ_{SFR} allowed by our data. The Σ_{mol}–τ_{orb} relationship and Σ_{mol} itself do not look significantly influenced by stellar mass (Fig. 3f).

5 TIME-SCALE PROFILES

Radial profiles of the time-scales studied in this work give further insights. In Fig. 4 we analyse time profiles as the azimuthal averages of τ_{dep}^{mol} and τ_{orb} for each Hubble type. The figure shows the radial variation of the molecular depletion time (τ_{dep}^{mol}, first row), orbital time (τ_{orb}, second row), and the ratio between the two time-scales (third row) within radial bins of $0.2\,R_{gal}/R_e$. In the fourth row, we plot the two time-scale azimuthal averages against each other.

The panel (a) of the figure illustrates the behaviour of the median of the depletion time for each category. The global average profile (the thick black line) increases of about 0.5 dex from the centre to $2\,R_e$; the increase between one radius bin and the following is only 0.1 dex, though. A more significant gradient (1 dex from the centre to the outskirt of the galactic discs) was observed by Wong (2009) for a smaller sample of nearby star-forming galaxies. Utomo et al. (2017) show that depletion time increases, decreases, or does not change in the centre of face-on galaxies in the EDGE sample.[4] Those behaviours seem to follow the trends of the Σ_{SFR} profiles with the galactic radius. The authors attribute those changes to different dynamical pressure equilibriums between the galaxies induced by large dynamics (from barred and interacting systems) or local changes of stellar mass surface density. Molecular gas mass surface densities, instead, do not appear influenced by the same effects.

[4] Utomo et al. (2017) include only EDGE galaxies with inclination below 75°.

Downloaded from https://academic.oup.com/mnras/article-abstract/475/2/1791/4743749
by University of Durham - Stockton Campus user
on 13 March 2018

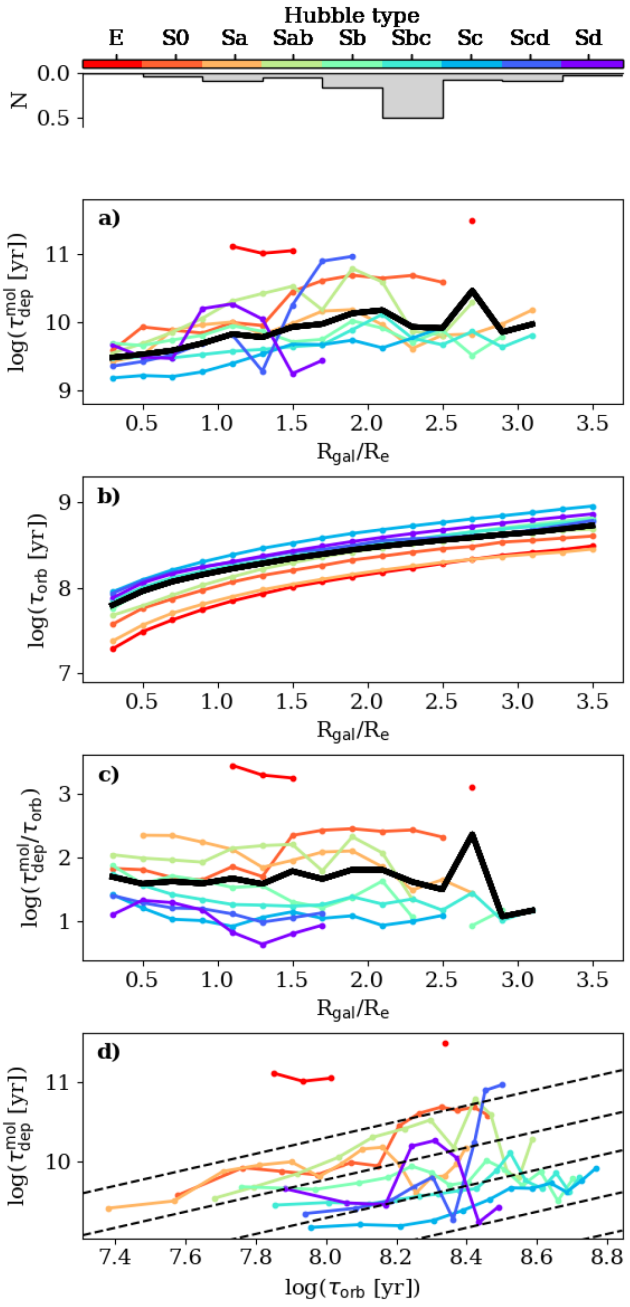

Figure 4. The azimuthal averages of τ_{dep}^{mol} (panel a), τ_{orb} (panel b), $\tau_{dep}^{mol}/\tau_{orb}$ (panel c) as a function of effective radii. The azimuthal average is defined as the median of the quantities in a particular morphological type within the radial bins of $0.2\,R_{gal}/R_e$. Panel (d) shows the azimuthal average of τ_{dep}^{mol} versus τ_{orb} where the dashed lines indicate constant orbital efficiencies of 0.5 per cent, 1.7 per cent, 5 per cent, 17 per cent, and 50 per cent. The solid black lines in panels (a), (b), and (c) are the average (median) profiles of the sample. The histogram on the top row of the figure indicates the relative fractions of pixels within a particular Hubble category. This figure shows that the molecular depletion time profiles from early-type (late-type) galaxies tend to be located above (below) the sample average, while the opposite behaviour is observed in the orbital time azimuthal averages.

The orbital time profiles (Fig. 4, panels c and d) are obtained from our JAM modelling and are thus smooth, slowly increasing from the centre to the outskirts of the galaxies. The average ratio between the two time-scales is generally flat around ∼1.5 consistent with an orbital efficiency $\epsilon_{orb} \sim 5$ per cent.

Regarding the Hubble type, the molecular depletion times of early- and late-type galaxies are well separated in most of the cases (e.g. Fig. 4a). The radial profiles of E, S0, and Sab galaxies are above the global average, while the radial profiles of Sb, Sbc, Scd galaxies are below the global average value. Nevertheless, the global average does not segregate early- and late types at every radii. Sd galaxy profile shows an increase above the global average between ∼0.7 and ∼1.3 R_e, where the depletion time assumes values very similar to early-type galaxies (i.e. $\tau_{dep}^{mol} \sim 10^{10}$ yr). Scd galaxy profile displays a similar increment between ∼1.3 to ∼2 R_e, where the depletion time is slightly below $\sim 10^{11}$ yr. For the earliest (E) and latest (Sd) types we possess only a few measurements (see histogram on the top of Fig. 4), therefore their profiles might suffer of sample bias.

In the panel (b), early-type galaxies show orbital times shorter than the sample average, while for late-type objects the times are longer than this value. In the panel (c), the ratio of time-scales appears completely segregated by morphology around the average sample profile.

The last panel of Fig. 4 shows the azimuthal averages of two time-scales against each other. In most of the cases, the radial increase of τ_{orb} is tracked by an increase in τ_{dep}^{mol}, while the Sd profile are a notable exception. The Sbc profile, in particular, follows closely the orbital efficiency of 5 per cent, meaning that this galaxy type drives the resolved relationship between τ_{dep}^{mol} and τ_{orb}. Indeed, Sbc galaxies dominate the total amount of detected lines of sight in our sample. In general, the correlations with the Hubble type that we see through this analysis closely resembles to the pixel-by-pixel behaviour of the previous sections even when H I is accounted (see Appendix C).

In summary, we observe that the galaxy morphologies are correlated to both the molecular depletion time and the orbital time of the galaxies. As a consequence, galaxies with different morphologies have different slopes in the τ_{dep}^{mol}–τ_{orb} relation. This behaviour is mostly driven by Σ_{SFR}, because Σ_{mol} in our sample does not seem to correlate with either the orbital time or morphologies.[5] The observed segregations are not simply driven by the stellar mass, even though it has an important contribution in setting the molecular depletion time of the galaxies.

6 DISCUSSION

The τ_{dep}^{mol}–τ_{orb} relation is supposed to represent a scenario where both growth of gravitational instabilities, the subsequent collapse of gas clouds, and ultimately star formation are influenced by the galactic rotation.

The existence of such a relation is not trivial, though. Star formation occurs exclusively within molecular clouds, which are local overdensities with respect to the molecular gas density distribution (for a recent review see Kennicutt & Evans 2012). Hence, Σ_{SFR} and Σ_{mol} can be considered as local quantities. The circular velocity, instead, depends on the mass within a certain galactocentric radius. The relationship between molecular depletion time and orbital time is therefore the parametrization of large-scale dynamics that acts on small scales.

[5] Note that our measurements are done within the CO map masked region. This masked region does not encompass the whole galaxy and favours regions where CO can be detected.

Downloaded from https://academic.oup.com/mnras/article-abstract/475/2/1791/4743749
by University of Durham - Stockton Campus user
on 13 March 2018

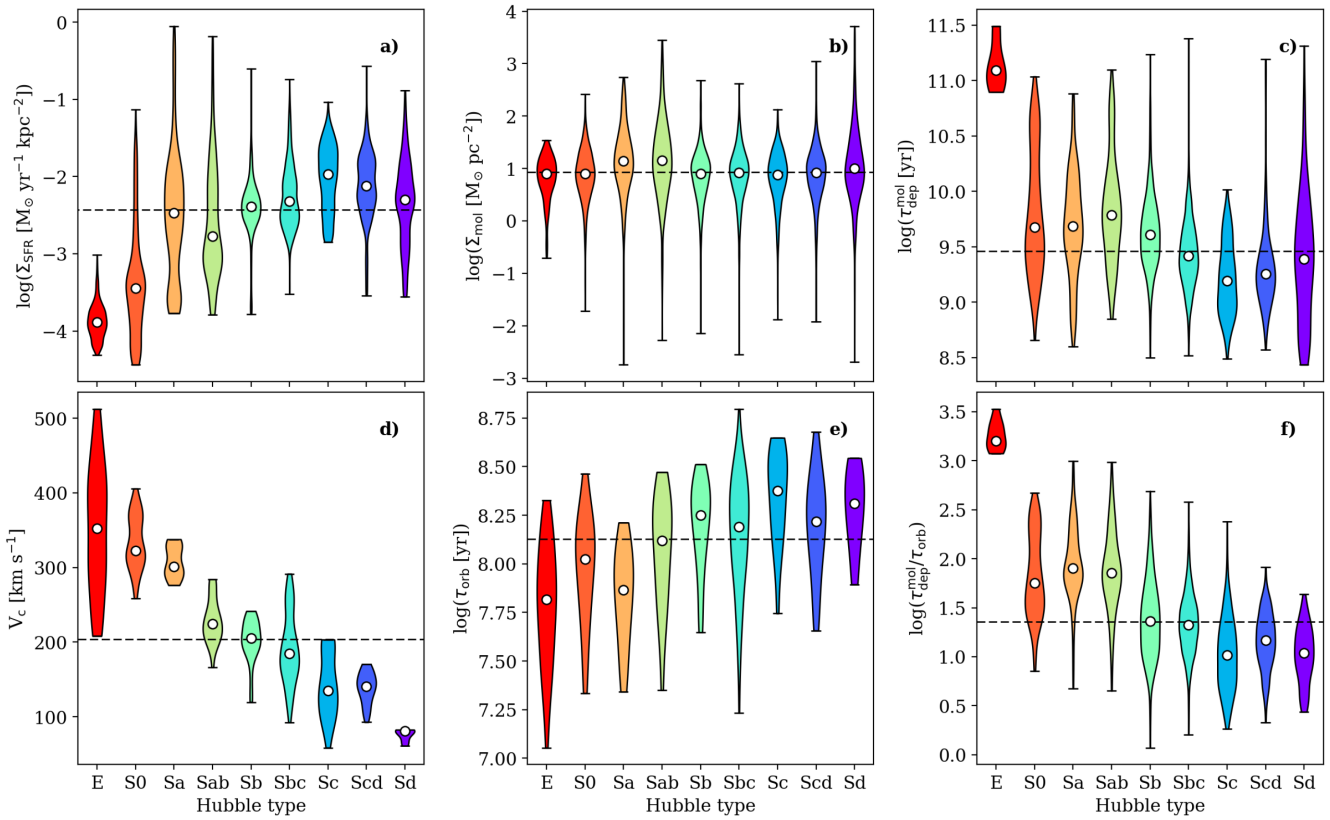

Figure 5. Violin plot representations of the resolved quantities that are studied in this paper across the Hubble types. Violin plots are histograms, where the width along the x-axis indicates the normalized fraction of data at the corresponding y-axis value. The values of $\Sigma_{\rm SFR}$, $\Sigma_{\rm mol}$, $\tau_{\rm dep}^{\rm mol}$, and $\tau_{\rm dep}^{\rm mol}/\tau_{\rm orb}$ are analysed pixel-by-pixel, while $V_{\rm c}$ and $\tau_{\rm orb}$ azimuthal averages are calculated within $2\,R_{\rm eff}$. Choosing $V_{\rm c}$ and $\tau_{\rm orb}$ within $1\,R_{\rm eff}$ renders the trend with Hubble type of the two quantities even more prominent. White circles represent the median values for each Hubble type. Dashed lines show the global median of the full sample of galaxies for a given property. This figure shows that all quantities, except $\Sigma_{\rm mol}$, appear to be related to the galactic morphology. These trends do not change if we include $\Sigma_{\rm mol}$ and $\Sigma_{\rm SFR}$ from the non-detected line of sights.

6.1 Morphological quenching in action?

Perhaps, the most striking manifestation of large-scale dynamics is represented by galaxy morphology, historically classified via Hubble type. Several works have shown that the Hubble types correlated with many galactic integrated properties (see e.g. Roberts & Haynes 1994; Consolandi 2017, and references therein). More recently the resolved study of González Delgado et al. (2015) observed that stellar metallicity, age, mass, and mass surface density increase monotonically from late- to early-type galaxies, while the opposite behaviour apparent in their SFRs (González Delgado et al. 2016). In line with these works, in Fig. 5, we summarize the resolved galactic properties analysed in this paper through morphology. On average, SFR surface density increases from early- to late-type morphologies, while the molecular depletion time decreases. The trend of $\tau_{\rm dep}^{\rm mol}$ with morphology has been noticed also by integrated studies (see e.g. Saintonge et al. 2011, their fig. 5). Instead, the average behaviour of the molecular gas surface density is generally flat with respect to the Hubble types. Previous studies have illustrated that early-type galaxies can encompass a large fraction of H_2 gas (e.g. Young, Bendo & Lucero 2009; Young et al. 2014). Nevertheless, we remind the reader that our sample is IR-selected, therefore the early-type objects analysed here might be more gas rich compared to 'standard' E or S0 galaxies.

The existence of a flat behaviour of $\Sigma_{\rm mol}$ with respect to Hubble type might indicate that a significant reservoir of molecular gas is present in every galaxy of our sample, but in our early types the cold gas has lost the ability to form stars (e.g. Martig et al. 2013). The suppression of star formation in galaxies is generally referred as 'quenching'. Star formation quenching has been explained using a variety of effects (see the introduction of Martig et al. 2009 for a quick summary).

In particular, together with the conclusions of González Delgado et al. (2015), our evidence supports the idea of 'morphological quenching,' where a gaseous disc embedded within a stellar spheroid, rather than a stellar disc, becomes stable against gravitational collapse (e.g. Martig et al. 2009). This scheme does not envision a shortage of molecular gas, in line with what we observed in our data. Instead, the suppression of the disc instabilities is the cause of the star formation shutdown even if a substantial amount of gas is present.

Other explanations can apply too. Quenching introduced by AGN feedback (e.g. Cattaneo et al. 2009) might have an effect, since ∼35 per cent of our targets host an AGN. The discrepancy in the star formation rate along the Hubble sequence can be also enhanced due to the particular conditions within the late-type galaxies. In those systems, high-mass star formation (mini-starburst events) can trigger feedback causing the destruction of the clouds, but also compression of the interstellar gas that creates new overdensities and increases star formation (Saintonge et al. 2011). We cannot exclude also the possibility that our early-type galaxies require

Downloaded from https://academic.oup.com/mnras/article-abstract/475/2/1791/4743749
by University of Durham - Stockton Campus user
on 13 March 2018

a lower-than-Galactic α_{CO} to deduce the right Σ_{mol} values (see Appendix D).

6.2 Stabilization via shear

The morphological quenching model is based on the Toomre (1964) theory, which predicts that the development of gravitational instabilities within the gaseous disc is hampered by the gas kinematics and by the presence of dissipative forces induced by the galaxy differential rotation, as shear.

Shear as a stabilizing agent against self-gravity has been invoked several times to explain the differences of cloud properties between observations and simulations (e.g. Dobbs & Pringle 2013; Colombo et al. 2014; Suwannajak et al. 2014; Miyamoto et al. 2015; Ward et al. 2016). Hunter, Elmegreen & Baker (1998) defined a threshold in the gas mass surface density that sets a lower limit for the GMC formation which is directly proportional to the local shear rate. Meidt et al. (2015) showed that in M51, the cloud lifetime appears to be constrained by the shear rate in the inter-arm regions of the galaxy where this effect dominates over stellar feedback. Several works indicated that shear does not only set the locations where clouds can form, but also control star formation itself. Hydrodynamical simulations of Weidner, Bonnell & Zinnecker (2010) have shown that the formation of super star clusters is inversely proportional to the shear strength (see also Fogerty et al. 2016). The likelihood of OB associations formation is also disfavoured in this context. Similarly, Hocuk & Spaans (2011) observed that clouds subjected to high shear from supermassive black holes tends to have lower SFE. Davis et al. (2014) noticed some connection between shear strength and SFE in their sample of star-forming early-type galaxies. Weak rotational support might also be one of the main causes of starbursts in high-redshift systems. The low angular momentum of observed $z \approx 1$–3 objects is thought to reduce their stability and favour the generation of large clumps that substantially increases the star formation rate (see Obreschkow et al. 2015 and references therein). Nevertheless, star formation in the Milky Way clouds does not seem to correlate with shear at any stage of their evolution. Dib et al. (2012) discussed that shear might have an effect in setting where GMCs can form, but self-gravity is mainly balanced by other factors as stellar feedback, turbulence or magnetic field. The sharp decrement of the mean circular speed across the Hubble type (Fig. 5d; see also Kalinova et al. 2017b), together with the increment of the orbital time (Fig. 5e), suggests that a different degree of shear is present within the different morphologies.

We can explicitly calculate the local shear rate within our galaxies through the Oort's constant A:

$$A = 0.5 \left(\frac{V_c}{R_{gal}} - \frac{dV_c}{dR_{gal}} \right) = \frac{\pi}{\tau_{orb}}(1 - \beta), \quad (16)$$

where $\beta = d\ln V_c / d\ln R_{gal}$ represents the shape of the circular speed curve. Assuming that the rising part of the curve behaves as a solid body, $V_c \propto R_{gal}$, this gives $\beta = 1$ and $A = 0$, while in the flat part of the curve, V_c =constant, $\beta = 0$, and the shear reaches its maximum at $A = \pi/\tau_{orb}$. In the top-left panel of Fig. 6, we plot the average depletion time versus the average azimuthal shear (A) for each Hubble type. Clearly, the molecular depletion time follows the increment of A across the Hubble types within the detected lines of sight, where the late-type galaxies have lower τ_{dep}^{mol} and less shear than the early types. Moreover, the averaged τ_{dep}^{mol} and A are strongly correlated across the Hubble types, showing a Spearman rank of $r = 0.9$. This value decreases slightly to $r = 0.86$ when the elliptical galaxies are removed, because these galaxies only have a few detections. A similar (but weaker) correlation between the shear rates and morphologies have been observed also through integrated measurements (Seigar 2005). The top-right panel of Fig. 6 shows the azimuthal averaged values of β for each galaxy in our sample. The average β per morphology slightly decreases across the Hubble types ($r = -0.47$), which indicates again that the shear increases from late- to early types. Generally, $|\beta|$ is always below unity in Fig. 6 (right), meaning that, in the regions of the galaxies where we have detections, the contribution of the shear is never equal to zero. Therefore, according to equation (16), the shear behaviour is dominated by the behaviour of the orbital time in our sample. In Section 4 we observe that, on average, Σ_{SFR} increases with the orbital time across the Hubble types (see Fig 3b). In light of equation (16), this suggests that Σ_{SFR} is inversely proportional to the local shear as illustrated in Fig. 6 (bottom-left).

Given this, there does not appear to be a universal 'Silk–Elmegreen' law to appropriately describes the overall star formation in various morphologies of galaxies (at least on local scale), but a clear decrease of τ_{dep}^{mol}–τ_{orb} slope along the Hubble types is observed. Other parameters (such as shear) might need to be taken into account to obtain a universal star formation law (see also Tan 2000; Shi et al. 2011; Krumholz et al. 2012; Davis et al. 2014; Utreras, Becerra & Escala 2016; Bolatto et al. 2017). Nevertheless the violin plots in Fig. 5 show a large overlap, meaning that several regions in galaxies with different morphologies work in a similar way. The τ_{dep}^{mol}–τ_{orb} relation that we discussed in Section 3 might emerge due to the superposition of regions with similar local effects, but, not necessarily, belong to similar morphologies. In particular, spheroids and bulges are associated with discrepant data (Section 4 and Appendix B), as well the discrepant points with high metallicity, stellar surface density, and velocity dispersion (as seen in Appendix B). From this coincidence, it may be that the discs follow the τ_{dep}^{mol}–τ_{orb} relation while bulges and spheroids do not. However, these results are strongly shaped by our sample selection, so that this interpretation is not robust.

In conclusion, it appears that galaxy morphology affects both the capability of galaxies to form stars and the galaxy dynamics in a broad sense. The reverse causality may also be true: dynamical and gravitational instabilities may have an impact on SFR that can change the galaxy's appearance through secular processes (Khochfar & Silk 2006; Combes 2009).

7 SUMMARY

In this paper, we analyse the relation between molecular star formation efficiency and large-scale dynamics on the plane described by molecular depletion time and orbital time through a sample of 39 EDGE–CALIFA kpc-resolved galaxies (with $i < 65°$) spanning various morphological types, SFRs, molecular gas masses, and stellar masses. Our findings are summarized below.

(i) Considering all our detected lines of sight, $\tau_{dep}^{mol} \sim 20\tau_{orb}$ (i.e. 5 per cent of the available molecular gas is converted into stars at each orbit), with a large scatter of 0.5 dex (the left-hand panel of Fig. 2). This result is in agreement with previous findings by Kennicutt (1998), Wong & Blitz (2002), and Leroy et al. (2013).

(ii) The integrated measurements of molecular depletion time for Sb–Sbc type galaxies are moderately correlated with the orbital times at $2\,R_{eff}$ with a Spearman rank of ∼0.5–0.7 (the right-hand panel of Fig. 2). The early-type (E and S0) galaxies show very long depletion times, shifted away from the main τ_{dep}^{mol}–τ_{orb} relation.

Downloaded from https://academic.oup.com/mnras/article-abstract/475/2/1791/4743749
by University of Durham - Stockton Campus user
on 13 March 2018

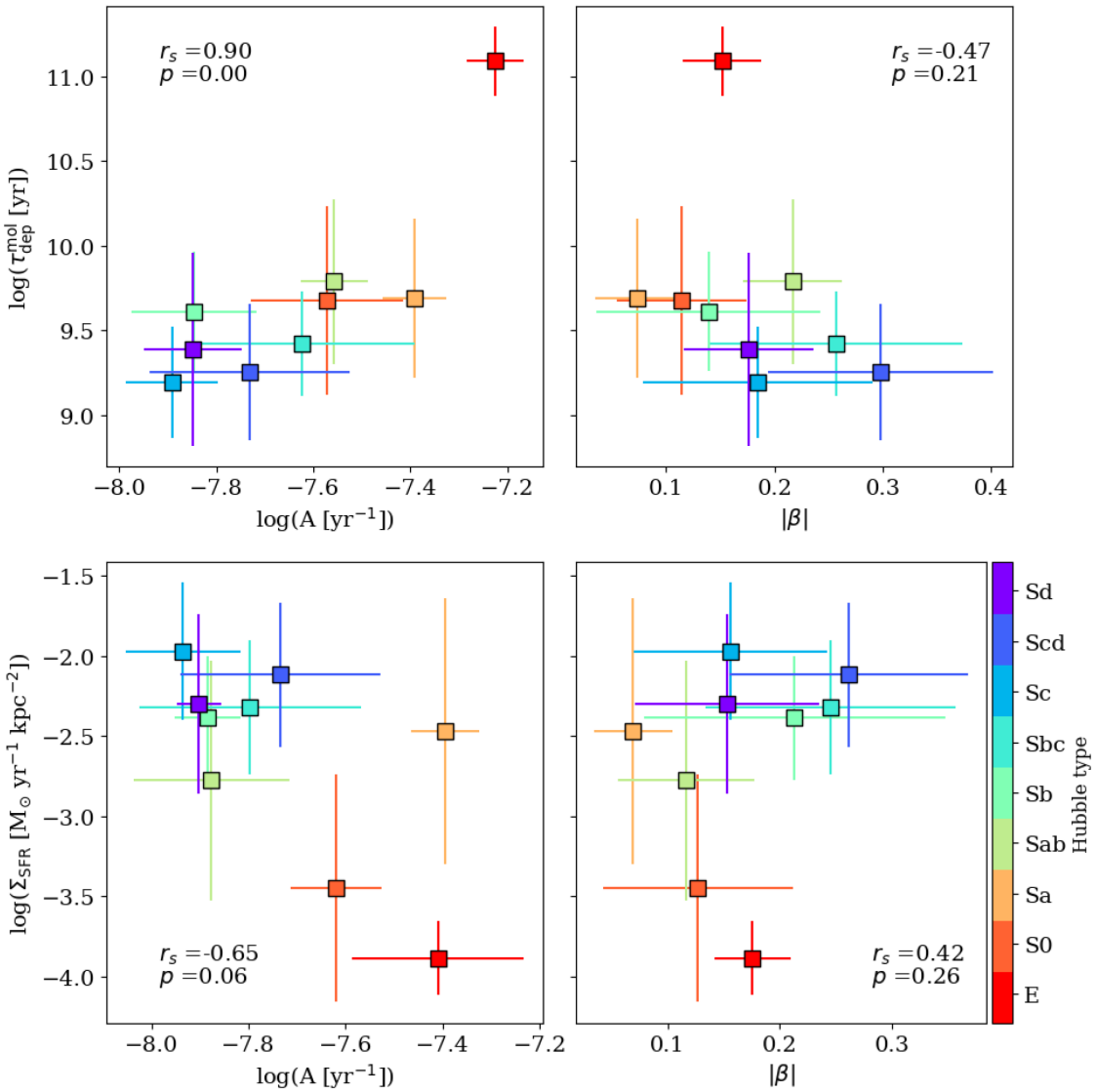

Figure 6. The correlations between the azimuthally averaged shear rate (A, left), the absolute value of the rotation curve shape (β, right), the molecular depletion time (top), and the SFR surface density (bottom) across the Hubble types where both dependent and independent quantities are defined. Coloured squares indicate the median of the quantity distributions within a given morphology, while the error bars show their median absolute deviations. In the corner of each panel, the Spearman rank (r_s) of each correlation is indicated together with the p-value (p). This figure shows that the average molecular depletion times and the SFR surface density are strongly correlated to the local shear across the Hubble types.

(iii) Galaxies with different Hubble types appear to follow different τ_{dep}^{mol}–τ_{orb} resolved relations that decrease in steepness from the early- to late types (Fig. 3). Alternatively, the Σ_{SFR}–τ_{orb} relation increases in steepness for later Hubble types. Those trends are less pronounced when binning the galaxies by their integrated stellar mass. On the other hand, the kpc-measurements of Σ_{mol} do not correlate with the Hubble types, suggesting that different τ_{dep}^{mol}–τ_{orb} relations across the Hubble types are driven by Σ_{SFR}, rather than Σ_{mol}. However, our conclusion may be affected by the infrared-bright criterion in the sample selection of the EDGE survey.

(iv) The azimuthal averages of molecular depletion times become shorter from early-type to late-type galaxies, while the opposite behaviour is observed for the orbital time (Fig. 4). As a result, the ratios between τ_{dep}^{mol} and τ_{orb} decrease from early-type to late-type galaxies (the bottom-right panel of Fig. 5).

(v) On average, the local shear rate appears to decrease across the Hubble types and appears to correlate with the molecular depletion times (Fig. 6), with a Spearman rank correlation coefficient of 0.9. This result provides a tentative evidence for a scenario where shear plays an important role in counteracting gravitational contraction and possibly suppressing star formation.

This study highlights also the urgency to gather a more homogeneous sample (in term of both galaxy morphologies and stellar masses) of kpc-resolved observations, together with the observations of molecular gas and optical IFU data at the scale of molecular clouds (∼50 pc), thereby connecting the global and local effects in a more consistent way.

ACKNOWLEDGEMENTS

The authors thank the anonymous referee for the useful insights that largely improved the quality of the paper. DC thanks Axel Weiss and Sharon Meidt for the stimulating discussions. DC acknowledges

Downloaded from https://academic.oup.com/mnras/article-abstract/475/2/1791/4743749
by University of Durham - Stockton Campus user
on 13 March 2018

support by the Deutsche Forschungsgemeinschaft, DFG through project number SFB956C. The works of DU and LB are supported by the National Science Foundation (NSF) under grants AST-1140063 and AST-1616924. ADB and RCL acknowledge support from NSF through grants AST-1412419 and AST-1615960. ADB also acknowledges visiting support by the Alexander von Humboldt Foundation. TW acknowledges support from NSF through grants AST-1139950 and AST-1616199. SFS acknowledges the PAPIIT-DGAPA-IA101217 project and CONACYT-IA-180125. ER is supported by a Discovery Grant from NSERC of Canada. SV acknowledges support from NSF AST- 1615960. HD acknowledges financial support from the Spanish Ministry of Economy and Competitiveness (MINECO) under the 2014 Ramón y Cajal program MINECO RYC-2014-15686. We acknowledge the usage of the HyperLeda data base (http://leda.univ-lyon1.fr). Support for the CARMA construction was derived from the states of California, Illinois, and Maryland, the James S. McDonnell Foundation, the Gordon and Betty Moore Foundation, the Kenneth T. and Eileen L. Norris Foundation, the University of Chicago, the Associates of the California Institute of Technology, and NSF. This research is based on observations collected at the Centro Astronomico Hispano Aleman (CAHA) at Calar Alto, operated jointly by the Max-Planck Institute for Astronomy (MPIA) and the Instituto de Astrofisica de Andalucia (CSIC). This research made use of Astropy, a community-developed core PYTHON package for Astronomy (Astropy Collaboration 2013).

REFERENCES

Accurso G. et al., 2017, MNRAS, 470, 4750
Alam S. et al., 2015, ApJS, 219, 12
Alatalo K. et al., 2013, MNRAS, 432, 1796
Astropy Collaboration, 2013, A&A, 558, A33
Bacon R. et al., 2001, MNRAS, 326, 23
Baldwin J. A., Phillips M. M., Terlevich R., 1981, PASP, 93, 5
Bigiel F., Leroy A., Walter F., Brinks E., de Blok W. J. G., Madore B., Thornley M. D., 2008, AJ, 136, 2846
Blitz L., Rosolowsky E., 2006, ApJ, 650, 933
Boissier S., Prantzos N., Boselli A., Gavazzi G., 2003, MNRAS, 346, 1215
Bolatto A. D., Wolfire M., Leroy A. K., 2013, ARA&A, 51, 207
Bolatto A. D. et al., 2017, ApJ, 846, 159
Bryant J. J. et al., 2015, MNRAS, 447, 2857
Bundy K. et al., 2015, ApJ, 798, 7
Caldú-Primo A., Schruba A., Walter F., Leroy A., Sandstrom K., de Blok W. J. G., Ianjamasimanana R., Mogotsi K. M., 2013, AJ, 146, 150
Calzetti D. et al., 2007, ApJ, 666, 870
Cappellari M., 2002, MNRAS, 333, 400
Cappellari M., 2008, MNRAS, 390, 71
Cappellari M. et al., 2011, MNRAS, 413, 813
Catalán-Torrecilla C. et al., 2015, A&A, 584, A87
Cattaneo A. et al., 2009, Nature, 460, 213
Chabrier G., 2003, PASP, 115, 763
Cid Fernandes R. et al., 2013, A&A, 557, A86
Cid Fernandes R. et al., 2014, A&A, 561, A130
Colombo D. et al., 2014, ApJ, 784, 3
Combes F., 2009, Mysteries of Galaxy Formation. Springer-Verlag, Berlin
Consolandi G., 2017, PhD thesis, Univ. Milano-Bicocca
Croom S. M. et al., 2012, MNRAS, 421, 872
Daddi E. et al., 2010, ApJ, 714, L118
Davis T. A. et al., 2013, MNRAS, 429, 534
Davis T. A. et al., 2014, MNRAS, 444, 3427
de Denus-Baillargeon M.-M., Hernandez O., Boissier S., Amram P., Carignan C., 2013, ApJ, 773, 173
Dib S., Helou G., Moore T. J. T., Urquhart J. S., Dariush A., 2012, ApJ, 758, 125
Dobbs C. L., Pringle J. E., 2013, MNRAS, 432, 653
Dobbs C. L., Burkert A., Pringle J. E., 2011, MNRAS, 413, 2935
Dopita M. A., Ryder S. D., 1994, ApJ, 430, 163
Elmegreen B. G., 1997, in Franco J., Terlevich R., Serrano A., eds, Rev. Mex. Astron. Astrofis. Conf. Ser. Vol. 6, Astrophysics: Starburst Activity in Galaxies. p. 165
Elmegreen B. G., Palouš J., Ehlerová S., 2002, MNRAS, 334, 693
Emsellem E., Monnet G., Bacon R., 1994, A&A, 285, 723
Emsellem E. et al., 2011, MNRAS, 414, 888
Falcón-Barroso J. et al., 2017, A&A, 597, A48
Fogerty E., Frank A., Heitsch F., Carroll-Nellenback J., Haig C., Adams M., 2016, MNRAS, 460, 2110
García-Benito R. et al., 2015, A&A, 576, A135
Genzel R. et al., 2010, MNRAS, 407, 2091
Gerhard O., 2002, Space Sci. Rev., 100, 129
González Delgado R. M. et al., 2014, A&A, 562, A47
González Delgado R. M. et al., 2015, A&A, 581, A103
González Delgado R. M. et al., 2016, A&A, 590, A44
Helfer T. T., Thornley M. D., Regan M. W., Wong T., Sheth K., Vogel S. N., Blitz L., Bock D. C.-J., 2003, ApJS, 145, 259
Heyer M. H., Corbelli E., Schneider S. E., Young J. S., 2004, ApJ, 602, 723
Hocuk S., Spaans M., 2011, A&A, 536, A41
Hughes A. et al., 2013, ApJ, 779, 46
Hunter D. A., Elmegreen B. G., Baker A. L., 1998, ApJ, 493, 595
Kalinova V., van de Ven G., Lyubenova M., Falcón-Barroso J., Colombo D., Rosolowsky E., 2017a, MNRAS, 464, 1903
Kalinova V. et al., 2017b, MNRAS, 469, 2539
Kennicutt R. C., Jr, 1989, ApJ, 344, 685
Kennicutt R. C., Jr, 1998, ApJ, 498, 541
Kennicutt R. C., Evans N. J., 2012, ARA&A, 50, 531
Kennicutt R. C., Jr, et al., 2007, ApJ, 671, 333
Kewley L. J., Dopita M. A., 2002, ApJS, 142, 35
Khochfar S., Silk J., 2006, MNRAS, 370, 902
Kim C.-G., Kim W.-T., Ostriker E. C., 2011, ApJ, 743, 25
Kim C.-G., Ostriker E. C., Kim W.-T., 2013, ApJ, 776, 1
Kroupa P., 2001, MNRAS, 322, 231
Kruijssen J. M. D., 2014, Class. Quantum Gravity, 31, 244006
Krumholz M. R., McKee C. F., 2005, ApJ, 630, 250
Krumholz M. R., Dekel A., McKee C. F., 2012, ApJ, 745, 69
Lablanche P.-Y. et al., 2012, MNRAS, 424, 1495
Leroy A. K., Walter F., Brinks E., Bigiel F., de Blok W. J. G., Madore B., Thornley M. D., 2008, AJ, 136, 2782
Leroy A. K. et al., 2009, AJ, 137, 4670
Leroy A. K. et al., 2013, AJ, 146, 19
Madau P., Dickinson M., 2014, ARA&A, 52, 415
Makarov D., Prugniel P., Terekhova N., Courtois H., Vauglin I., 2014, A&A, 570, A13
Martig M., Bournaud F., Teyssier R., Dekel A., 2009, ApJ, 707, 250
Martig M. et al., 2013, MNRAS, 432, 1914
McKee C. F., Ostriker E. C., 2007, ARA&A, 45, 565
Meidt S. E. et al., 2013, ApJ, 779, 45
Meidt S. E. et al., 2015, ApJ, 806, 72
Miyamoto Y., Nakai N., Kuno N., Seta M., Salak D., Kaneko H., Nagai M., Ishii S., 2015, in Iono D., Tatematsu K., Wootten A., Testi L., eds, ASP Conf. Ser. Vol. 499, Revolution in Astronomy with ALMA: The Third Year. Astron. Soc. Pac., San Francisco, p. 159
Monnet G., Bacon R., Emsellem E., 1992, A&A, 253, 366
Narayanan D., Krumholz M. R., Ostriker E. C., Hernquist L., 2012, MNRAS, 421, 3127
Neumann J. et al., 2017, A&A, 604, A30
Obreschkow D. et al., 2015, ApJ, 815, 97
Ostriker E. C., Shetty R., 2011, ApJ, 731, 41
Padoan P., Federrath C., Chabrier G., Evans N. J., II, Johnstone D., Jørgensen J. K., McKee C. F., Nordlund Å., 2014, in Beuther H., Klessen R. S., Dullemond C. P., Henning T., eds, Protostars and Planets VI. Univ. Arizona Press, Tucson, AZ, p. 77
Pearson K., 1901, Phil. Mag., 2, 559
Pérez E. et al., 2013, ApJ, 764, L1

Downloaded from https://academic.oup.com/mnras/article-abstract/475/2/1791/4743749
by University of Durham - Stockton Campus user
on 13 March 2018

Persic M., Salucci P., Stel F., 1996, MNRAS, 281, 27
Pety J. et al., 2013, ApJ, 779, 43
Rahman N. et al., 2011, ApJ, 730, 72
Rahman N. et al., 2012, ApJ, 745, 183
Regan M. W., Thornley M. D., Helfer T. T., Sheth K., Wong T., Vogel S. N., Blitz L., Bock D. C.-J., 2001, ApJ, 561, 218
Reina-Campos M., Kruijssen J. M. D., 2017, MNRAS, 469, 1282
Roberts M. S., Haynes M. P., 1994, ARA&A, 32, 115
Saintonge A. et al., 2011, MNRAS, 415, 61
Sánchez S. F. et al., 2012, A&A, 538, A8
Sánchez S. F. et al., 2014, A&A, 563, A49
Sánchez S. F. et al., 2016, A&A, 594, A36
Sandstrom K. M. et al., 2013, ApJ, 777, 5
Schmidt M., 1959, ApJ, 129, 243
Schruba A. et al., 2011, AJ, 142, 37
Seigar M. S., 2005, MNRAS, 361, L20
Semenov V., Kravtsov A., Gnedin N., 2017, ApJ, 845, 133
Shi Y., Helou G., Yan L., Armus L., Wu Y., Papovich C., Stierwalt S., 2011, ApJ, 733, 87
Silk J., 1997, ApJ, 481, 703
Suwannajak C., Tan J. C., Leroy A. K., 2014, ApJ, 787, 68
Tacconi L. J. et al., 2010, Nature, 463, 781
Tan J. C., 2000, ApJ, 536, 173
Tan J. C., 2010, ApJ, 710, L88
Tasker E. J., Tan J. C., 2009, ApJ, 700, 358
Toomre A., 1964, ApJ, 139, 1217
Utomo D. et al., 2017, ApJ, 849, 26
Utreras J., Becerra F., Escala A., 2016, ApJ, 833, 13
Walcher C. J. et al., 2014, A&A, 569, A1
Walter F., Brinks E., de Blok W. J. G., Bigiel F., Kennicutt R. C., Jr, Thornley M. D., Leroy A., 2008, AJ, 136, 2563
Wang B., Silk J., 1994, ApJ, 427, 759
Ward R. L., Benincasa S. M., Wadsley J., Sills A., Couchman H. M. P., 2016, MNRAS, 455, 920
Weidner C., Bonnell I. A., Zinnecker H., 2010, ApJ, 724, 1503
Wong T., 2009, ApJ, 705, 650
Wong T., Blitz L., 2002, ApJ, 569, 157
Wong T. et al., 2013, ApJ, 777, L4
Wyse R. F. G., 1986, ApJ, 311, L41
Wyse R. F. G., Silk J., 1989, ApJ, 339, 700
York D. G. et al., 2000, AJ, 120, 1579
Young L. M., Bendo G. J., Lucero D. M., 2009, AJ, 137, 3053
Young L. M. et al., 2014, MNRAS, 444, 3408

SUPPORTING INFORMATION

Supplementary data are available at *MNRAS* online.

Table 1. The sample of nearby EDGE–CALIFA galaxies considered in this work.

Please note: Oxford University Press is not responsible for the content or functionality of any supporting materials supplied by the authors. Any queries (other than missing material) should be directed to the corresponding author for the article.

APPENDIX A: TESTING THE EFFECTS OF NON-DETECTIONS

In Section 4 we observed that, binned through their morphology, $\tau_{\rm dep}^{\rm mol}$ and $\tau_{\rm orb}$ line-of-sight averages are anticorrelated, while $\Sigma_{\rm SFR}$ and $\tau_{\rm orb}$ correlate. Instead, $\Sigma_{\rm mol}$ does not show any significant trend

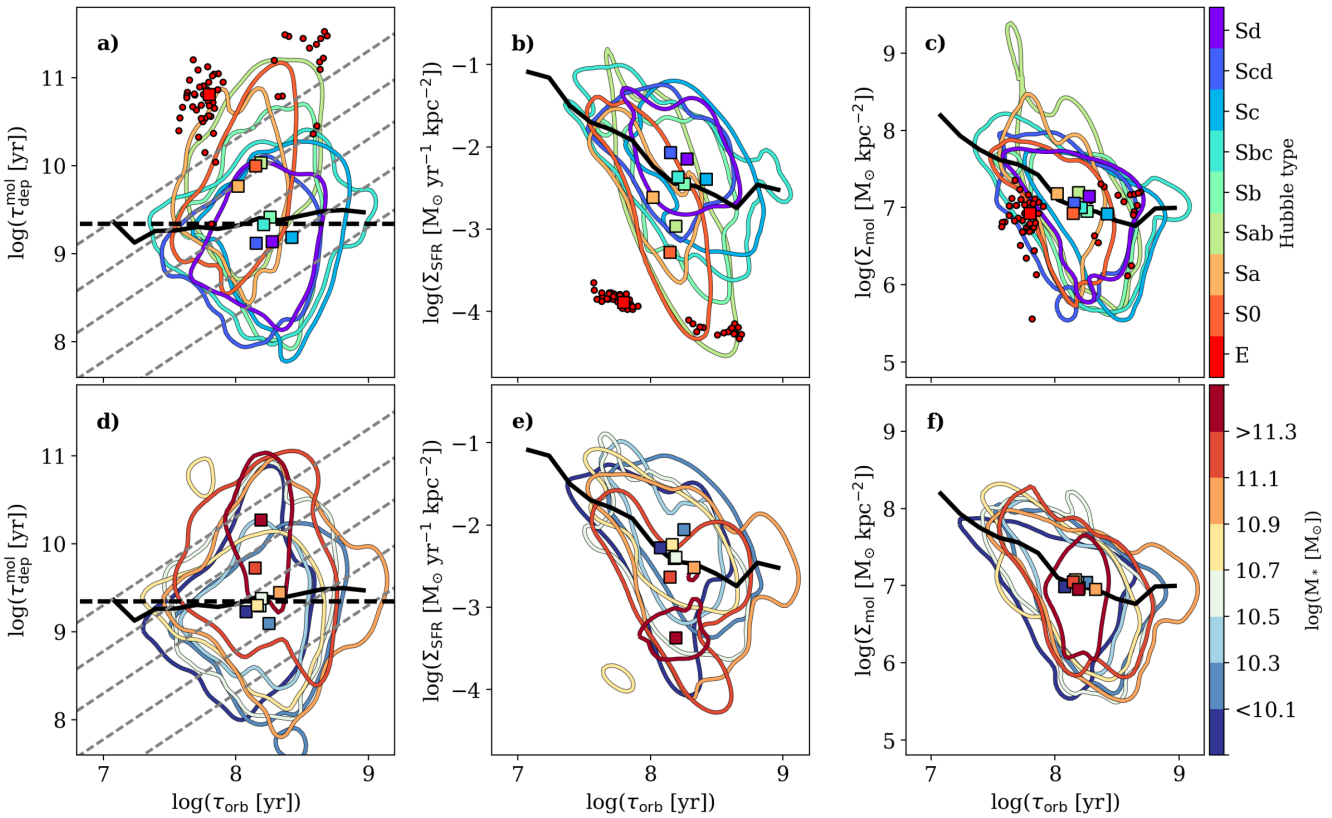

Figure A1. Pixel-by-pixel relations between $\tau_{\rm dep}^{\rm mol}$ (first column), $\Sigma_{\rm SFR}$ (second column), and $\Sigma_{\rm mol}$ (third column) with respect to $\tau_{\rm orb}$ colour-encoded with Hubble type (first row) and integrated stellar mass (second row) where molecular depletion time non-detections are added. Symbols and notations follow Fig. 3. $\Sigma_{\rm mol}$ non-detections are the most significant. The increased scatter in the $\tau_{\rm dep}^{\rm mol}$–$\tau_{\rm orb}$ relationship, however, does not change the main conclusion of the paper regarding the role of morphology in the dynamics and star formation properties of the galaxies.

Downloaded from https://academic.oup.com/mnras/article-abstract/475/2/1791/4743749
by University of Durham - Stockton Campus user
on 13 March 2018

with both orbital time and Hubble type. To understand how non-detections could affect those behaviours, we reproduce Fig. 3 including Σ_{SFR} and Σ_{mol} lower limits. The result is shown in Fig. A1. In Section 3 we observed, for example, that the addition of the depletion time non-detections yielded no discernible correlation between τ_{dep}^{mol} and τ_{orb} when observed pixel-by-pixel.

Mainly the non-detections affect the τ_{dep}^{mol} and Σ_{mol} trends of late-type galaxies (from Sb to Sd) for which relation contours extend to lower times and surface densities, respectively (Fig. A1 panels a and c). Elliptical galaxies show several new data points at longer orbital times. In this representation, the late-type galaxies do not show a clear τ_{dep}^{mol}–τ_{orb} relation. The Σ_{SFR}–τ_{orb} diagram is not largely affected by those values, though (Fig. A1b). Together, the behaviour of the early-type galaxies remains significantly different from the late types and the average behaviours observed through detections only are largely preserved.

In a similar way, the inclusion of non-detections does not alter our conclusions about the role of the stellar mass in the trends noticed through detections only via Hubble type. In Section 4 we observed a weak (anti-) correlation between the average (Σ_{SFR}) τ_{dep}^{mol} and τ_{orb}. In Fig. A1 (second row) those behaviours look less defined. As for the galaxy morphologies, we do not distinguish any clear trends when Σ_{mol} is considered (Fig. A1f).

APPENDIX B: TESTING THE INFLUENCE OF LOCAL GALACTIC PROPERTIES

In this paper, we use the nebular emission lines surveyed by CALIFA to obtain information about the star formation in the galaxies. CALIFA also observed the stellar spectra, which can be used to characterize the stellar population properties, including the mass surface densities, metallicities, ages, and stellar kinematics (see Cid Fernandes et al. 2013, 2014; Pérez et al. 2013; González Delgado et al. 2014 for further details). Here, we study how the relation between the molecular depletion time and the orbital time is influenced by local properties. To do so, we approach the problem on two fronts: by considering (1) the properties of the stellar population, and (2) the kinematics within galaxies. For this study, we consider the detections only, because the contours related to detections plus non-detections provide similar conclusions.

Following Bolatto et al. (2017, their figs 17 and 18), we divide the sample into two subsamples based on the properties under study. The results of our analysis are illustrated in Fig. B1. We plot in blue (red) the data with values below (above) the property median. We also use yellow circles to show measurements obtained within the bulge area as described by the effective radius calculated by Neumann et al. (2017). In general, the overlapping region between the upper and lower hand distributions contains the majority of the points (90−95 per cent of the total). However, outliers also give useful insights.

The stellar mass surface density is the local property that appears to have the most direct influence on both depletion and orbital times (Fig. B1a). The medians of the lower and upper hand distributions (red and blue squares in the panel) closely follow the running average between τ_{dep}^{mol} and τ_{orb} (full black line in the panel). Lower orbital times are dominated by high values of Σ_*. The converse is also true when we consider the non-detections (thin coloured lines in the plot). The data are not, however, separate across the lines of

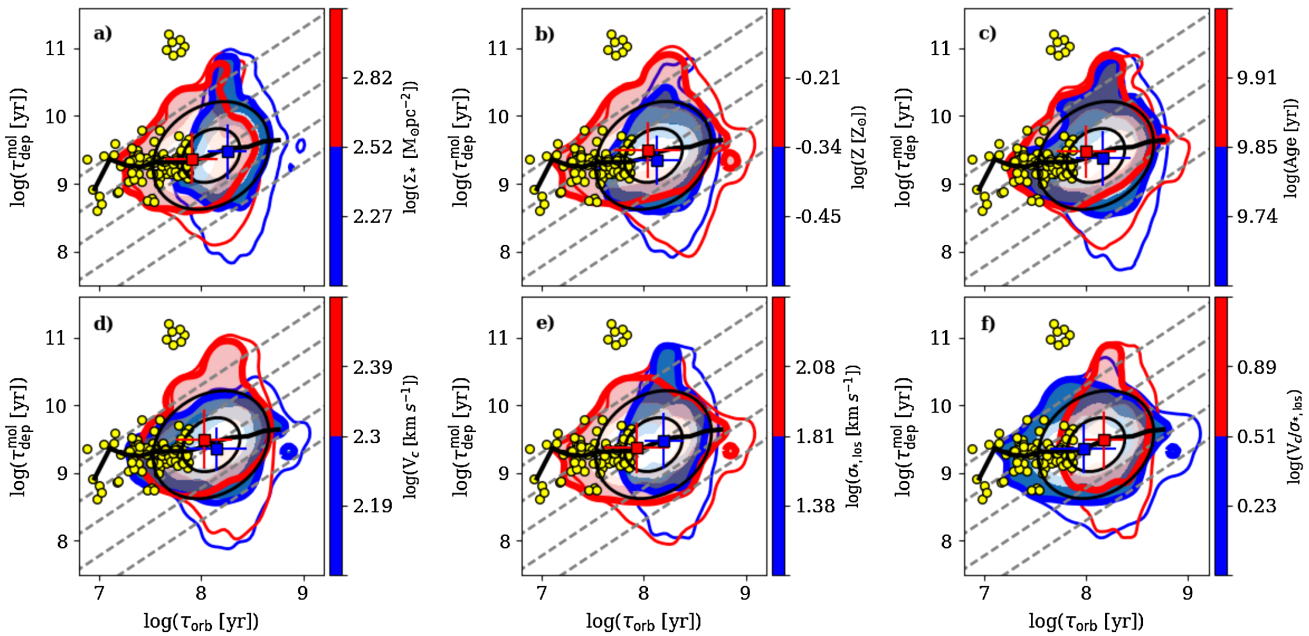

Figure B1. Analysis of the distribution of local stellar properties in the τ_{dep}^{mol}–τ_{orb} diagram: stellar mass surface density (panel a), metallicity (panel b), age (panel c), circular speed (panel d), line-of-sight stellar velocity dispersion (panel e), and line-of-sight stellar order-over-random motion (panel f). The data points are separated according to their colour-encoding property medians. The contour shades contain 50 per cent, 75 per cent, and 95 per cent of the total number of detections. The outer thick (thin) coloured contour contains 95 per cent of the detections (detections plus non-detections), while the coloured squares show the median of τ_{dep}^{mol} and τ_{orb} within the respective distributions with their respective standard deviations (for the detection only). The black solid lines indicate median of the related quantities within bins of 0.2 dex with respect to τ_{orb}. The confidence ellipsoids shown in black contain ∼68 per cent and ∼95 per cent of the total number of detections. Grey dashed diagonal lines indicate constant orbital efficiency (ϵ_{orb}): from the top to bottom 0.5 per cent, 1.7 per cent, 5 per cent, 17 per cent, and 50 per cent. Yellow circles indicate the measurements obtained within the bulge area delimited by the bulge effective radius (Neumann et al. 2017). The figure shows that the scatter is mainly given by data points with high values of Σ_*, stellar metallicity, and velocity dispersion generally attributable to nuclei, bulges, or spheroids.

Downloaded from https://academic.oup.com/mnras/article-abstract/475/2/1791/4743749
by University of Durham - Stockton Campus user
on 13 March 2018

constant depletion time. This means that both star formation rate and molecular mass surface densities are correlated with Σ_*. The stellar mass surface density is also partially connected with the orbital efficiency: low efficiencies appear dominated by high Σ_* values and vice versa. The outliers of the relation (i.e. the data points outside the outer confidence ellipsoid) show mainly anomalous Σ_* values. The stellar mass surface density represents the local gravitational potential, therefore a connection with $\tau_{\rm orb}$, which in turn parametrizes the global potential at a particular galactocentric radius, is expected. Several authors (e.g. Leroy et al. 2008; Bolatto et al. 2017) have also noticed that the depletion time anticorrelates with Σ_*. This is foreseen by a picture of feedback-regulated star formation (e.g. Ostriker & Shetty 2011), where the dynamical-equilibrium pressure is correlated with $\Sigma_{\rm SFR}$. The molecular-to-atomic to gas ratio is also proportional to the hydrostatic pressure in the disc mid-plane (e.g. Wong & Blitz 2002; Blitz & Rosolowsky 2006), and this quantity is covariant with the stellar mass surface density (Kim, Ostriker & Kim 2013).

Fig. B1b partitions the $\tau_{\rm orb}$–$\tau_{\rm dep}^{\rm mol}$ data by metallicity. Again, most data overlap between the populations, but the outliers are associated with high metallicity, specifically high $\tau_{\rm dep}^{\rm mol}$ and low $\tau_{\rm orb}$, and (considering the non-detections also) the high orbital time data all show metallicity values in the high-metallicity group. Interestingly, the detections with a metallicity in the lower half of the distribution are tightly constrained within the 95 per cent confidence ellipsoid. The lower orbital efficiency shown in the plot ($\epsilon_{\rm orb} = 0.5$ per cent) is fully dominated by high-metallicity values. Indeed, the median related to the high-metallicity distribution seems slightly shifted towards low orbital efficiencies and vice versa. The same is true if we consider the behaviour of the stellar age across the relation (Fig. B1c). In this case, however, the contours that contain 95 per cent of the data for both distributions appear co-spatial in the diagram. If we include non-detection too, the lines of sight belonging to the lower age data extend to lower depletion time values.

Stellar kinematics give further insights. Interestingly, different values of circular speed are distributed across all different values of orbital times (Fig. B1d), meaning that the orbital time per pixel is mainly driven by the galactocentric radius. Depletion times above 10^{10} yr are located only towards high $V_{\rm c}$ values. This result reflects what observed in Bolatto et al. (2017; their fig. 18), where high stellar mass lines of sight dominate high $\tau_{\rm dep}^{\rm mol}$ region in their plots. The medians of $\tau_{\rm orb}$ and $\tau_{\rm dep}^{\rm mol}$ within the two distributions closely resemble the medians when the relation is colour-encoded by stellar metallicity or age.

Instead, the behaviour of the stellar velocity dispersion (σ_*) is similar to the behaviour of Σ_* (Fig. B1e). Again outliers appear dominated by high-velocity dispersion lines of sight. The trend of the ordered-over-random motion of the stars mirrors the σ_* behaviour (Fig. B1f) and it is clearly driven by the velocity dispersion.

Lines of sight within the identified galactic bulge areas (Neumann et al. 2017) are primarily found as outliers in these diagrams, particularly within the upper distributions of stellar mass surface density, metallicity, and velocity dispersion.

In conclusion, it appears that outliers of the $\tau_{\rm dep}^{\rm mol}$–$\tau_{\rm orb}$ relation are generally dominated by high values of Σ_*, σ_*, and, in particular, stellar metallicity. These properties are associated with galaxy nuclei, bulges, and spheroids. These outliers are also found in data from early-type galaxies, where these structures are dominant (see Fig 3a). Stellar surface density and velocity dispersion closely follow the trend of the relation, while we have some indications that high metallicity, ages, and circular speeds belong to lines of sight shifted towards low $\epsilon_{\rm orb}$ and vice versa.

APPENDIX C: TESTING THE INFLUENCE OF ATOMIC GAS

Kennicutt–Schmidt and Silk–Elmegreen relations have been originally measured for the total neutral gas which incorporate both molecular and atomic gas, the latter generally traced via 21 cm wavelength line observations. In this section, we test how the inclusion of the atomic gas would potentially change the Silk–Elmegreen type relation that we analysed in this paper. Since the resolved H I measurements do not exist for our sample, we generate synthetic atomic mass surface density by imposing $\Sigma_{\rm HI} = 10\,{\rm M}_\odot\,{\rm pc}^{-2}$ for each pixel, corrected for the physical size of the pixel. This is justified by previous results. For example, Leroy et al. (2008) showed that the radial profiles of atomic mass surface density are remarkably constant around $10\,{\rm M}_\odot\,{\rm pc}^{-2}$ (see their Appendix F) in a sample of

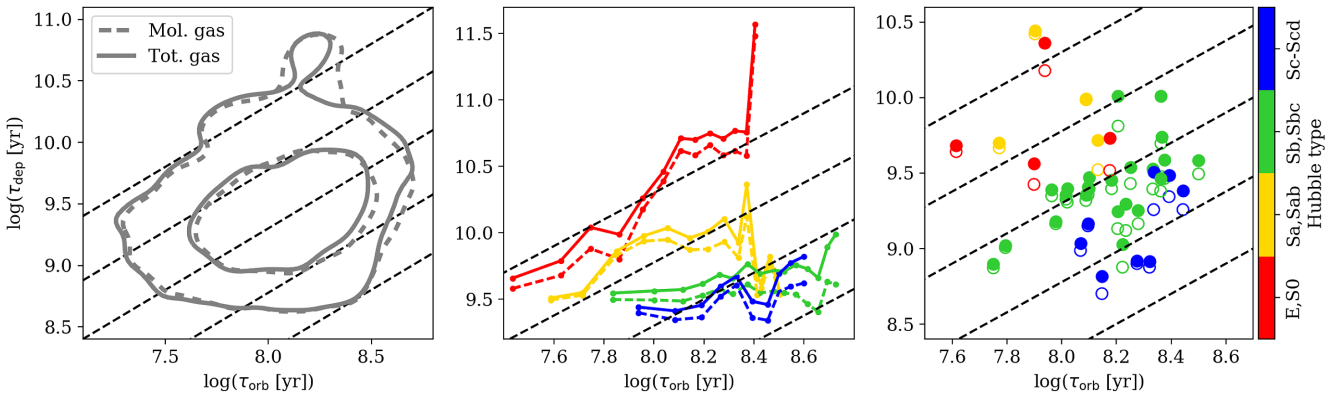

Figure C1. The depletion time–orbital time relations explored in the paper with synthetic atomic gas measurements added. *Left:* pixel-by-pixel $\tau_{\rm dep}$–$\tau_{\rm orb}$ relations from total (atomic plus molecular; grey full lines) and molecular (grey dashed lines) gas. The inner and outer contours contain 66 per cent and 95 per cent of the total detected CO lines of sight, respectively. *Middle:* azimuthal averages of $\tau_{\rm dep}$ and $\tau_{\rm orb}$ in radial bins of $0.2\,R_{\rm gal}/R_{\rm e}$ where total gas (full lines) and molecular gas only (dashed lines) are included in the calculation of $\tau_{\rm dep}$, divided into Hubble type groups. The last group, 'Sc–Sd', considers 'Scd' galaxies too. *Right:* total (full symbols) and molecular (empty symbols) gas depletion times integrated within $2R_{\rm e}$ with respect to orbital time measurements at $2R_{\rm e}$. Each symbol represents a given galaxy colour-encoded according to its Hubble type group. In the panels, dashed black straight lines indicate constant conversion efficiencies, from top to bottom, of 0.5 per cent, 1.7 per cent, 5 per cent, 17 per cent, and 50 per cent. The addition of the atomic gas does not appear to significantly alter the main conclusions of our analysis of the $\tau_{\rm dep}^{\rm mol}$–$\tau_{\rm orb}$ relationship.

Downloaded from https://academic.oup.com/mnras/article-abstract/475/2/1791/4743749
by University of Durham - Stockton Campus user
on 13 March 2018

23 nearby star-forming galaxies drawn from THINGS (Walter et al. 2008) and HERACLES (Leroy et al. 2009). Fig. C1 shows the result of the test, which considers detections only. Generally, the addition of the atomic gas does not change the appearance of pixel-by-pixel relation originally observed in Fig. 2 (see Fig. C1, left). The inner contours of the relations that include 66 per cent of data points from total and molecular gas only (full and dashed lines, respectively) follow the 5 per cent orbital efficiency line. This might be related to the fact that most of our galaxies appear to be molecular dominated, since in 75 per cent of our pixels $\Sigma_{\rm mol} > \Sigma_{\rm H\,I}$ across all sampled galactocentric radii. The middle panel of Fig. C1 shows the azimuthal average profiles of the total (full lines) and molecular (dashed lines) gas depletion time profiles with respect to the orbital time profiles divided into Hubble type groups. Total and molecular-only gas profiles track each other quite well in each morphology group, with the total gas profiles always shifted towards slightly longer depletion times. Integrated quantities in the rightmost panel of the figure mirror this behaviour. The anticorrelation with orbital times across the Hubble sequence is present whether total or molecular gas depletion times are considered. Nevertheless, vertical shift between the two depletion times is more prominent in some galaxies than in others and does not necessarily follows the morphological type. Summarizing, the conclusions concerning the correlation between galactic morphology, orbital time, and depletion time discussed along the paper are preserved by including the atomic gas contribution in the analysis, despite the representation used. However, since atomic gas-dominated surface densities do not correlate with $\Sigma_{\rm SFR}$ (e.g. Schruba et al. 2011), the relation between total gas depletion time and orbital time might be associated with the conversion between H I to H_2 rather than to star formation itself. In particular the creation of molecular gas overdensities from the smooth atomic medium in the regions of the galaxies (where the gas self-gravity overcomes tidal forces and shear) might happen on the orbital time-scale. Nevertheless, we are not able to discern between the two different interpretations with the current data.

APPENDIX D: CAVEATS

Sample biases. EDGE was designed to span larger values of stellar masses and morphologies than previous surveys. Nevertheless, the CARMA sample was selected based on IR-brightness, which leads to a lack of well-resolved E and Sd types, as well as galaxies with stellar mass below $10^9\,{\rm M}_\odot$ and above $10^{11}\,{\rm M}_\odot$. We further restricted the sample to galaxies with inclination $<65^\circ$ and with good dynamical models. We ended up with a sample of 39 galaxies and 6360 individual lines of sight, each representing a ∼kpc-scale region. Of these, 80 per cent belong to Sab-to-Sc morphologies, and the remaining 20 per cent are equally shared between the other Hubble types. The percentage of Sab-to-Sc data points decreases to 75 per cent if non-detections are considered. At the same time, galaxies with stellar masses between 10^{10} and $10^{11}\,{\rm M}_\odot$ dominate the data (74 per cent), while we have only few measurements for low-mass galaxies (6 per cent for $M_* < 10^{10}\,{\rm M}_\odot$) and for high-mass galaxies (20 per cent for $M_* > 10^{11}\,{\rm M}_\odot$). However, we find that these results do not change if we consider non-detections and that the sample used in this paper is representative of the inclination-limited EDGE sample (see Section 2.3).

Flux recovery. EDGE cubes do not include the total power data. The observing strategy, which incorporates data from CARMA's D- and E-configurations, allows the recovery of a large range of scales (see Bolatto et al. 2017). However, we cannot be sure about how the addition of the total power might influence the non-detections. Along the paper we observe that including the lower limits (especially of $\Sigma_{\rm mol}$) can change the results we derive. In particular, CO non-detections add shorter depletion times to our measurements which results in no discernible correlation between $\tau_{\rm dep}^{\rm mol}$ and $\tau_{\rm orb}$. Total power data might boost $\Sigma_{\rm mol}$ non-detections to larger values which would reestablish the relationship we observe through detections only. Therefore, our results regarding the $\tau_{\rm dep}^{\rm mol}$–$\tau_{\rm orb}$ relation and its variation with respect to the morphology of the galaxies need to be verified with a more homogeneous sample of targets and a more complete reconstruction of emission from the interferometer data.

CO-to-H_2 conversion factor variation. For our sample, we derive the molecular gas mass surface densities from CO luminosities using a constant, Galactic conversion factor: $\alpha_{\rm CO} = 4.4\,{\rm M}_\odot\,{\rm pc}^{-2}\,({\rm K\,km/s\,pc}^2)^{-1}$. Bolatto, Wolfire & Leroy (2013; see also Accurso et al. 2017) discuss that one of the main sources of influence of the CO-to-H_2 conversion factor is the metallicity. Low metallicity reduces the H_2 self-shielding that, in turn, decreases the quantity of available CO. Therefore, low-metallicity galaxies require a larger $\alpha_{\rm CO}$ to derive a correct molecular gas mass from the observed CO emission. The global gas-phase metallicities of our galaxies are almost indistinguishable from the Solar value of $12 + \log[{\rm O/H}] = 8.7$. Nevertheless, this effect may be important for the local measurements that show values significantly lower than the Galactic average (see e.g. Fig. B1) and might require larger values of $\alpha_{\rm CO}$ to obtain the right $\Sigma_{\rm mol}$. We do not believe that this bias dominates our results because the lowest gas-phase metallicity data points do not correspond to the lowest $\Sigma_{\rm mol}$ values.

The usage of a constant $\alpha_{\rm CO}$ might not be appropriate for all galaxy morphologies. Massive galaxies tend to have stronger interstellar radiation field and higher gas velocity dispersion than low-mass ones, which would increase the CO emission we measure. Those galaxies would require a lower-than-Galactic $\alpha_{\rm CO}$ to produce the correct amount of molecular gas mass. This would result in lower values of $\tau_{\rm dep}^{\rm mol}$ for this kind of galaxies. Considering Fig. 5, in order to have, in early-type galaxies, molecular depletion times comparable to the global average we would need an $\alpha_{\rm CO}$ ∼2–3 times lower than Galactic for Sa and S0 galaxies, respectively. We do not consider elliptical galaxies since we have too few detections for a robust conclusion. Here, we have taken the Milky Way as a Sbc galaxy (Gerhard 2002), where Sbc galaxies dominate our $\tau_{\rm dep}^{\rm mol}$ sample average. Given an uncertainty of ∼0.3 dex on the generally assumed $\alpha_{\rm CO}$ (Bolatto, Wolfire & Leroy 2013), it is plausible that the flat trend of $\Sigma_{\rm mol}$ we observe with respect to Hubble type is caused by our choice of a constant CO-to-H_2 conversion factor.

Another aspect, discussed in Leroy et al. (2013) and Sandstrom et al. (2013), is the possibility that galaxy centres have lower $\alpha_{\rm CO}$. This would lead to lowering the value of the depletion time at small galactocentric radii. At the same time, galaxy centres tend to have shorter orbital times. In this sense, by using a customized $\alpha_{\rm CO}$ in particular regions of the galaxies would result in a better correlation between $\tau_{\rm dep}^{\rm mol}$ and $\tau_{\rm orb}$ as observed in Leroy et al. (2013, their section 4.4).

JAM versus CO rotation curves. To test how the usage of dynamical models instead of CO rotation curves might influence our conclusions about the $\tau_{\rm dep}^{\rm mol}$–$\tau_{\rm orb}$ relation, we collect 13 galaxies (2234 data) with both dynamical models and well-defined CO rotation curves, and we derive the orbital times for both of them. For this experiment we use only detections. CO rotation curve models have been calculated via the universal rotation curve formula presented in Persic, Salucci & Stel (1996) (Levy et al. in preparation for more details). In Fig. D1 we plot the $\tau_{\rm dep}^{\rm mol}$–$\tau_{\rm orb}$ relation

Downloaded from https://academic.oup.com/mnras/article-abstract/475/2/1791/4743749
by University of Durham - Stockton Campus user
on 13 March 2018

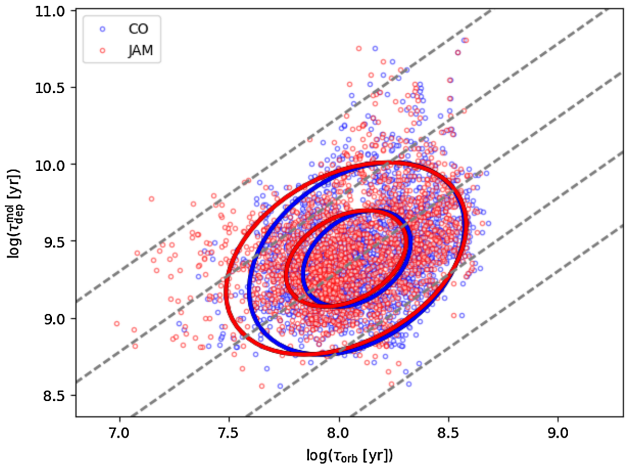

Figure D1. Pixel-by-pixel $\tau_{\rm dep}^{\rm mol}$–$\tau_{\rm orb}$ relations where orbital time is obtained with the JAM dynamical model (red) and CO rotation curves (blue). Dashed lines and confidence ellipses follow the convention of Fig. 2. The choice of rotation curve modelling does not significantly change the results.

obtained through JAM- and CO-derived CVCs. Confidence ellipses related to JAM appear shifted towards lower orbital times by ∼0.1 dex. This might be because the JAM approach tends to overestimate the mass-to-light ratio, therefore the circular velocity, in the centre of the galaxies. This has been reported in several occasions: face-on barred systems (Lablanche et al. 2012) or when averaging several stellar populations (Davis et al. 2013). At the same time, CO rotation curves are severely affected by beam smearing at lower galactocentric radii, which underestimates velocities in those regions. Nevertheless, the same relationship between molecular depletion time and orbital time emerges from the CO-based rotation curves, so we conclude that this choice does not strongly affect our results. Most of the data overlap and the relations derived by the two modelling approaches are well described by the 5 per cent efficiency line with a 0.5 dex scatter.

Inclination and distance. Some of the trends we observe may be influenced by galactic biases. To check this, in the first and second rows of Fig. D2, we plot the SE law data colour-encoded by galactic inclination and distance, respectively. For this test we use only detections.

For the inclination test, we include the full sample of galaxies at any inclination (where this work so far has only considered $i < 65^{\circ}$). High orbital times are dominated by highly inclined galaxies. The same is true for data with very low H_2 mass and SF surface densities, besides the deprojection of the surface density for the inclination (see Utomo et al. 2017). Depletion time seems less dominated by this parameter. However, the highest $\Sigma_{\rm SFR}$ and $\Sigma_{\rm mol}$ values are found in low inclination galaxies.

Although CALIFA has been designed as a diameter-limited survey to reduce the effect of the distance biases, the distance to the galaxies none the less appears to have some impact on the relations. The more distant objects dominate very high depletion time measurements ($>10^{10}$ yr). $\Sigma_{\rm SFR}$ and $\Sigma_{\rm mol}$ appear shifted towards lower values. Orbital times above $10^{8.5}$ yr, which constitute the prominent outliers, are located in the same bin. For the closest objects, instead, we can measure some of the lowest depletion time values, and the highest SFRs and H_2 masses per unit area of the sample. From the inclination and distance tests we conclude that the detection criteria select different data for different galaxy types and environments. The scaling with distance suggests that we may be detecting a small scale-dependent effect at the kpc-scales, but our data lack the spatial dynamic range to explore this extensively. These tests suggest small shifts in the typical galaxies in each population, however, the fundamental relationships still show the same basic trends no matter how the data are divided or selected.

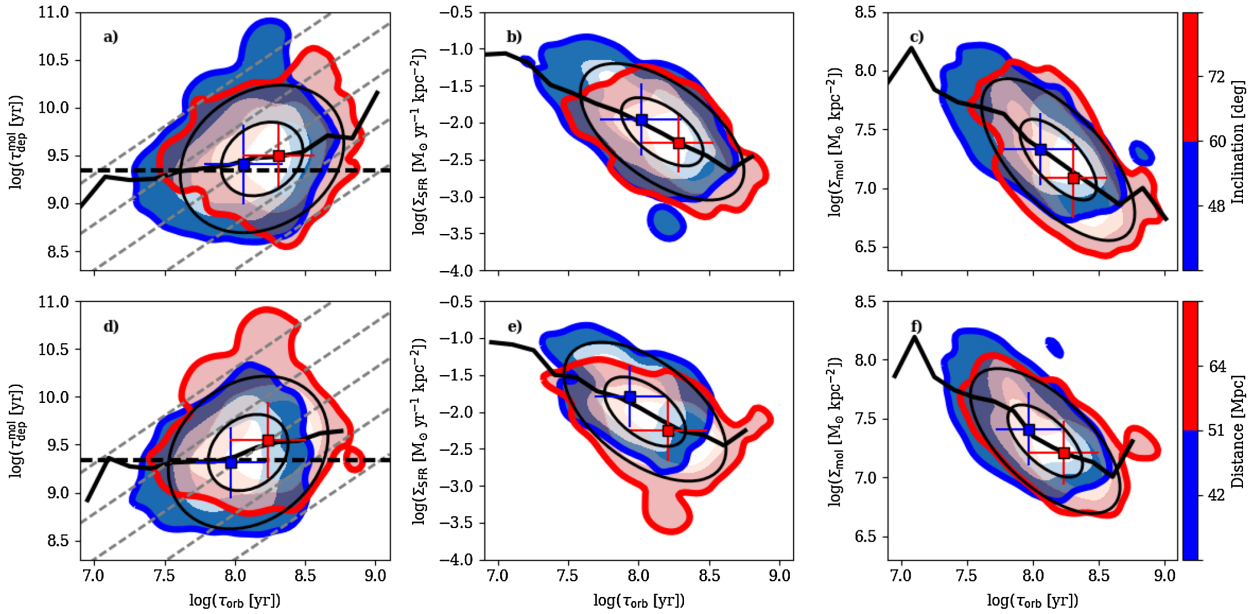

Figure D2. Relationships between $\tau_{\rm dep}^{\rm mol}$, $\Sigma_{\rm SFR}$, and $\Sigma_{\rm mol}$ with respect to the orbital time colour-encoded by inclination (first row) and distance (second row). Symbols and notations follow Fig. B1.

This paper has been typeset from a TEX/LATEX file prepared by the author.

Downloaded from https://academic.oup.com/mnras/article-abstract/475/2/1791/4743749
by University of Durham - Stockton Campus user
on 13 March 2018